

# Cosmic evolution of the CIV in high-resolution hydrodynamic simulations

E. Tescari<sup>1,2,3\*</sup>, M. Viel<sup>1,2</sup>, V. D’Odorico<sup>1</sup>, S. Cristiani<sup>1,2</sup>, F. Calura<sup>1,4</sup>, S. Borgani<sup>1,2,3</sup> and L. Tornatore<sup>1,2,3</sup>

<sup>1</sup> *INAF - Osservatorio Astronomico di Trieste, Via G.B. Tiepolo 11, I-34131 Trieste, Italy*

<sup>2</sup> *INFN/National Institute for Nuclear Physics, Via Valerio 2, I-34127 Trieste, Italy*

<sup>3</sup> *Dipartimento di Fisica - Sezione di Astronomia, Università di Trieste, Via G.B. Tiepolo 11, I-34131 Trieste, Italy*

<sup>4</sup> *Jeremiah Horrocks Institute for Astrophysics and Supercomputing, University of Central Lancashire, Preston PR1 2HE*

16 July 2021

## ABSTRACT

We investigate the properties of triply ionized Carbon (CIV) in the Intergalactic Medium (IGM) using a set of high-resolution and large box-size cosmological hydrodynamic simulations of a  $\Lambda$ CDM model. We rely on a modification of the public available Tree-Smoothed Particle Hydrodynamics (SPH) code GADGET-2 that self-consistently follows the metal enrichment mechanism by means of a detailed chemical evolution model. We focus on several numerical implementations of galactic feedback: galactic winds in the energy driven and momentum driven prescriptions, galactic winds hydrodynamically coupled to the surrounding gas and Active Galactic Nuclei (AGN) powered by gas accretion onto massive black holes. Furthermore, our results are compared to a run in which galactic feedback is not present and we also explore different initial stellar mass function. After having addressed some global properties of the simulated volume like the impact on the star formation rate and the content in Carbon and CIV, we extract mock IGM transmission spectra in neutral hydrogen (HI) and CIV and perform Voigt profile fitting. The results are then compared with high-resolution quasar (QSO) spectra obtained with the UVES spectrograph (Ultra Violet Echelle Spectrograph) at the VLT (Very Large Telescope) and the High Resolution Echelle Spectrometer (HIRES) at Keck. We find that feedback has little impact on statistics related to the neutral hydrogen, while CIV is more affected by galactic winds and/or AGN feedback. The feedback schemes investigated have a different strength and redshift evolution with a general tendency for AGN feedback to be more effective at lower redshift than galactic winds. When the same analysis is performed over observed and simulated CIV lines, we find reasonable good agreement between data and simulations over the column density range  $N_{\text{CIV}} = 10^{12.5-15} \text{ cm}^{-2}$ . Also the CIV line-widths distribution appears to be in agreement with the observed values, while the HI Doppler parameters,  $b_{\text{HI}}$ , are in general too large showing that the diffuse cosmic web is heated more than what is inferred by observations. The simulation without feedback fails in reproducing the CIV systems at high column densities at all redshift, while the AGN feedback case agrees with observations only at  $z < 3$ , when this form of feedback is particularly effective. We also present scatter plots in the  $b - N$  and in the  $N_{\text{CIV}} - N_{\text{HI}}$  planes, showing that there is rough agreement between observations and simulations only when feedback is taken into account.

Although it seems difficult to constrain the nature and the strength of galactic feedback using the present framework and find a unique model that fits all the observations, these simulations offer the perspective of understanding the galaxy-IGM interplay and how metals produced by stars can reach the low density IGM.

**Key words:** methods: numerical – galaxies: formation – intergalactic medium – quasars: absorption lines – cosmology: theory

## 1 INTRODUCTION

The interplay between galaxies and the intergalactic medium (IGM) is a fundamental and poorly understood aspect in the stan-

\* E-mail: tescari@oats.inaf.it

dard scenario of structure formation. The intimate connection between the diffuse IGM and the baryons that populate star forming galaxies can shed light on the metal enrichment of the IGM (its nature and redshift evolution), on the properties of galactic feedback and on the evolution of the ultraviolet background.

In recent years, this field has benefitted from spectroscopical observations of quasar (QSO) and Gamma Ray Burst (GRB) spectra (both at high and low resolution) and from photometric and spectroscopical information on high redshift galaxies in the same field of view. This has in turn allowed us to perform cross-correlation studies of absorption lines and properties of galaxies (e.g. Steidel et al. 2010, and references therein). Observations have revealed that the IGM is polluted with heavy elements such as Carbon, Oxygen and Silicon (e.g. Weymann et al. 1981; Cowie et al. 1995; Aguirre et al. 2005). Furthermore, high redshift star forming galaxies have been shown to interact with the surrounding medium by powering strong galactic outflows (e.g. Adelberger et al. 2005). The IGM enrichment mechanism is, however, still poorly constrained and the extent of metal pollution of the low density IGM, or around Lyman-break galaxies, controversial (e.g. Schaye et al. 2000a; Pieri et al. 2006; Porciani & Madau 2005).

Among many different metal species, the doublet produced by triply ionized carbon (CIV) is the one that has been most widely studied since it is relatively easy to identify in the regions redward of Lyman- $\alpha$  emission. CIV has been observed from low-redshift up to very high redshift (Ryan-Weber et al. 2006, 2009; Becker et al. 2009); its clustering properties in the transverse direction and along the line-of-sight have been investigated (D’Odorico et al. 2002; Pichon et al. 2003; Tytler et al. 2009) along with the global evolution of the CIV density fraction down to  $z < 2$  (D’Odorico et al. 2010); the optical depth in CIV has been derived using pixel-optical-depth techniques applied to the UVES Large Programme sample in order to constrain the metallicity of the low density gas (Schaye et al. 2003; Aracil et al. 2004); the cross-correlation between galaxies and CIV properties have also been addressed in great detail using either Keck or UVES spectra (Simcoe et al. 2006; Scannapieco et al. 2006). The general conclusion is that CIV absorption systems are indeed related to outskirts of galactic haloes but it is still unclear whether the gas producing the absorption is enriched by nearby galaxies or at an earlier epoch by smaller objects.

The large amount of data available has prompted the implementation of relevant physical processes into sophisticated hydrodynamic codes in order to simulate both galaxies and QSO/GRB absorption lines. The first attempt to model CIV properties using hydrodynamic simulations has been made by Haehnelt et al. (1996). Subsequently, it has been demonstrated that a key ingredient that appears to be necessary in order to reproduce CIV metal line statistics is feedback in the form of galactic winds (Theuns et al. 2002; Cen et al. 2005; Oppenheimer & Davé 2006, 2008). Galactic winds triggered by supernovae (SN) explosions have been modelled in a simple way using mainly two schemes that conserve either energy or momentum (Oppenheimer & Davé 2006; Tescari et al. 2009). Other sources of feedback like Active Galactic Nuclei (AGN) has also been considered to address global gas properties from high to low redshift (Tornatore et al. 2010). A second very important ingredient has been the implementation of accurate chemical evolution models that self-consistently follow the release of different metal species from stars and also allow for different initial stellar mass functions (Tornatore et al. 2007; Kawata & Rauch 2007; Kobayashi et al. 2007; Sommer-Larsen & Fynbo 2008; Wiersma et al. 2009; Oppenheimer et al. 2009; Wiersma et al. 2010; Davé et al. 2010; Cen & Chisari 2010).

This is a second paper in a series that exploits the capabilities of a state-of-the-art modification of the public available code GADGET-2 (Springel 2005). In the first paper we addressed neutral hydrogen properties (Tescari et al. 2009) focusing in particular on Damped Lyman- $\alpha$  systems. In this paper we study the CIV transition by extending the feedback models simulated.

This paper is organized as follows. In Sections 2 and 3 we present, respectively, the observational data sample and our set of simulations along with the different feedback models implemented in our code. In Section 4 we compare some global properties of the simulations: the cosmic star formation rate and the evolution of the total Carbon content. We then focus on the neutral hydrogen statistics in Section 5. In Sections 6 and 7 we investigate the CIV column density distribution function and the evolution with redshift of the CIV cosmological mass density,  $\Omega_{\text{CIV}}$ , respectively. In Section 8 we study the probability distribution function of the CIV Doppler parameter and, in Section 9, we present the CIV column density-Doppler parameter relation. The last part of the paper is dedicated to the analysis of the HI-CIV correlated absorption (Section 10). Finally, in Section 11 we summarize our main results and we draw some conclusions.

## 2 OBSERVATIONAL DATA SAMPLE

The core of the observational data sample is formed by the high resolution ( $R \sim 45000$ ), high signal-to-noise (S/N) QSO spectra obtained with the UVES spectrograph (Dekker et al. 2000) at the Kueyen unit of the ESO VLT (Cerro Paranal, Chile) in the framework of the ESO Large Programme (LP): “The Cosmic Evolution of the IGM” (Bergeron et al. 2004).

We have used the sample of HI Lyman- $\alpha$  absorption lines described in Saitta et al. (2008) and D’Odorico et al. (2008), which is based on 18 objects of the LP plus 4 more QSOs of which: J2233-606 and HE1122-1648 were observed with UVES, while HS1946+7658 and B1422+231 were obtained with the High Resolution Echelle Spectrometer (HIRES) at the Keck Telescope at comparable resolution and signal-to-noise ratio. In this work, also the HI Lyman- $\alpha$  list of the QSO Q0055-269, observed with UVES, has been added to the sample. The adopted sample of CIV absorptions was described in D’Odorico et al. (2010). The previous group of QSOs was increased with the addition of the UVES spectra of PKS2000-330 and PKS1937-101 to extend the redshift interval to  $z \gtrsim 3$ .

All UVES spectra were reduced with the UVES pipeline following the standard procedure. The continuum level was determined by interpolating with a cubic spline the region of the spectrum free from evident absorption features. Absorption lines were fitted with Voigt profiles using the context LYMAN of the MIDAS reduction package (Fontana & Ballester 1995). A minimum number of components was adopted to fit the velocity profile in order to reach a normalized  $\chi^2 \sim 1$ . For all the QSO in the sample, the Lyman- $\alpha$  forest was defined as the interval between the Lyman- $\beta$  emission plus  $1000 \text{ km s}^{-1}$  (to avoid contamination from the Lyman- $\beta$  forest), and  $5000 \text{ km s}^{-1}$  from the Lyman- $\alpha$  emission; the CIV forest was defined as the interval between the Lyman- $\alpha$  emission and  $5000 \text{ km s}^{-1}$  from the CIV emission. The higher bound was fixed to avoid the proximity region affected by the QSO emission, where most of the intrinsic systems are found.

CIV features are distinguished into *components* or *lines*, meaning the velocity components in which every absorption profile has been decomposed, and *systems*, formed by groups of com-

QSO	$z_{\text{em}}$	$\Delta z_{\text{Ly}\alpha}$	$\Delta z_{\text{CIV}}$
HE 1341-1020	2.142	1.6599-2.090	1.467-2.090
Q0122-380	2.2004	1.709-2.147	1.513-2.147
PKS 1448-232	2.224	1.729-2.171	1.531-2.171
PKS 0237-23	2.233	1.737-2.179	1.538-2.179
J2233-606	2.248	1.7496-2.194	1.550-2.194
HE 0001-2340	2.265	1.764-2.211	1.564-2.211
HS 1626+6433 <sup>a</sup>	2.32		1.607-2.265
HE 1122-1648 <sup>b</sup>	2.40	1.878-2.344	1.665-2.344
Q0109-3518	2.4057	1.883-2.349	1.674-2.349
HE 2217-2818	2.414	1.888-2.355	1.681-2.355
Q0329-385	2.435	1.9096-2.378	1.697-2.378
HE 1158-1843	2.448	1.919-2.391	1.707-2.391
HE 1347-2457	2.5986	2.046-2.539	1.826-2.539
Q1442+2931 <sup>a</sup>	2.661		1.875-2.600
Q0453-423	2.669	2.106-2.608	1.881-2.608
PKS 0329-255	2.696	2.129-2.635	1.902-2.635
HE 0151-4326	2.763	2.186-2.701	1.955-2.701
Q0002-422	2.769	2.191-2.707	1.959-2.707
HE 2347-4342	2.880	2.285-2.816	2.067-2.816
SBS 1107+487 <sup>a</sup>	2.966		2.114-2.900
HS 1946+7658 <sup>c</sup>	3.058	2.435-2.991	2.181-2.991
HE 0940-1050	3.0932	2.465-3.025	2.214-3.025
Q0420-388	3.1257	2.493-3.057	2.239-3.057
S4 0636+68 <sup>a</sup>	3.175		2.278-3.106
SBS 1425+606 <sup>a</sup>	3.199		2.297-3.129
PKS 2126-158	3.292	2.633-3.221	2.370-3.221
B1422+231 <sup>b</sup>	3.623	2.914-3.546	2.630-3.546
Q0055-269	3.66	2.945-3.583	2.659-3.583
PKS 2000-330	3.783		2.756-3.704
PKS 1937-101	3.787		2.770-3.400
PSS J1646+5514 <sup>a</sup>	4.059		2.972-3.975
PSS J1057+4555 <sup>a</sup>	4.131		3.029-4.046
BR 2237-0607 <sup>a</sup>	4.559		3.365-4.467

**Table 1.** Relevant properties of the QSOs forming the D’Odorico et al. (2010) observational sample. (a) QSOs from Boksenberg et al. (2003); (b) Reduced spectra kindly provided by T.-S. Kim; (c) Data from Kirkman & Tytler (1997).

ponents with relative separation smaller than  $dv_{\text{min}} = 50 \text{ km s}^{-1}$  (see D’Odorico et al. 2010, for a detailed description of the procedure). Both the velocity components and the systems in the sample have column densities in the range  $10^{11} \lesssim N_{\text{CIV}} \lesssim 10^{15} \text{ cm}^{-2}$ .

In order to further increase the number of CIV lines and to extend the sample to higher redshift, D’Odorico et al. (2010) have considered the CIV lines fitted in 9 QSO spectra observed with HIRES at Keck at a resolution and signal-to-noise ratio similar to those of their spectra and reported in Boksenberg et al. (2003). The fit with Voigt profiles was carried out by Boksenberg et al. (2003) with VPFIT<sup>1</sup>. The main difference between LYMAN and VPFIT is that the number of components fitted to a given velocity profile is, in general, larger using the latter (see also the discussion in Saitta et al. 2008). This is seen also in the analysis of D’Odorico et al. (2010), in particular from the comparison of the CIV lines detected in the spectrum of the QSO B1422+231, which is the only object in common between the two samples. D’Odorico et al. (2010) find that in all cases the number of components determined with VPFIT is larger or equal to that determined with LYMAN. However, when the total column density of each ab-

sorption system is considered the difference between the two fitting procedures becomes negligible.

All the QSOs of the observational sample are reported in Table 1 with their emission redshift and the redshift range covered by the Lyman- $\alpha$  forest and the CIV lines.

### 3 THE SIMULATIONS

In the following we review the main characteristics of the runs analysed in this work and we refer to Tescari et al. (2009) for a more extensive description of the simulations. Our code is the same modified version of the TreePM-SPH code GADGET-2 (Springel 2005) used in Tescari et al. (2009).

The simulations cover a cosmological volume (with periodic boundary conditions) filled with an equal number of dark matter and gas particles. The cosmological model chosen is a flat  $\Lambda$ CDM with the following parameters:  $\Omega_{\text{dm}} = 0.24$ ,  $\Omega_{\text{ob}} = 0.0413$ ,  $\Omega_{\Lambda} = 0.76$ ,  $n_s = 0.96$ ,  $H_0 = 73 \text{ km s}^{-1} \text{ Mpc}^{-1}$  and  $\sigma_8 = 0.8$ , which are in agreement with the latest results from large scale structure observables such as the cosmic microwave background, weak lensing, the Lyman- $\alpha$  forest and the evolution of mass function of galaxy clusters (Lesgourgues et al. 2007; Komatsu et al. 2009; Vikhlinin et al. 2009). The input linear dark matter power spectrum for the initial conditions has been generated at  $z = 99$  with CMBFAST (Seljak & Zaldarriaga 1996) and includes baryonic acoustic oscillations.

Radiative cooling and heating processes are modelled following the implementation of Katz et al. (1996). We assume a mean Ultra Violet Background (UVB) produced by quasars and galaxies as given by Haardt & Madau (1996), with the heating rates multiplied by a factor of 3.3 in order to better fit observational constraints on the temperature evolution of the intergalactic medium at high redshift (the factor of 3.3 was originally introduced because it gives a temperature at the mean cosmic density,  $T_0$ , in agreement with the Schaye et al. 2000b, data points). This background gives naturally  $\Gamma_{-12} \sim 0.8 - 1$  at low redshift, in agreement with recent observational measurements (Bolton et al. 2005; Faucher-Giguère et al. 2008). Multiplying the heating rates by the factor above (chosen empirically) results in a larger IGM temperature at the mean density which cannot be reached by the standard hydrodynamic code. This aims at mimicking, at least in a phenomenological way, the non-equilibrium ionization effects around reionization (see for example Ricotti et al. 2000; Schaye et al. 2000a; Bolton & Haehnelt 2007). A significant fraction in mass of the IGM resides in the tight power-law relation  $T = T_0(1 + \delta)^{\gamma-1}$  at around the mean density, where  $T_0$  is the temperature at the mean cosmic density and  $\delta$  the overdensity. Our reference simulations (see at the end of this Section), at redshift  $z = 3, 2.25$  and  $1.5$ , have  $\log(T_0(\text{K}))$ , respectively, equal to: 4.36, 4.33, 4.30 and  $\gamma$ , respectively, equal to: 1.58, 1.60, 1.62.

In our simulations, the standard multiphase star formation criterion of Springel & Hernquist (2003) is implemented, which contains an effective prescription for the inter-stellar medium (ISM). In this effective model, whenever the density of a gas particle exceeds a given threshold (set to  $\rho_{\text{th}} = 0.1 \text{ cm}^{-3}$  in terms of the number density of hydrogen atoms), that gas particle is flagged as star forming and is treated as multiphase. With this prescription baryons are in the form either a hot or a cold phase or in stars, thereby this density threshold marks the onset of cold clouds formation.

We follow self-consistently the evolution of these elements: H, He, C, O, Mg, S, Si and Fe. The contribution of metals is included

<sup>1</sup> <http://www.ast.cam.ac.uk/~rfc/vpfit.html>

Run	IMF	Box Size [ $h^{-1}$ Mpc]	$N_{\text{GAS}}$	$m_{\text{GAS}}$ [ $h^{-1} M_{\odot}$ ]	Softening [ $h^{-1}$ kpc]	Feedback
kr37edw500	Kroupa	37.5	$256^3$	$3.6 \times 10^7$	7.5	EDW
kr37mdw	Kroupa	37.5	$256^3$	$3.6 \times 10^7$	7.5	MDW <sup>a</sup>
kr37agn	Kroupa	37.5	$256^3$	$3.6 \times 10^7$	7.5	AGN <sup>b</sup>
kr37agn+edw300	Kroupa	37.5	$256^3$	$3.6 \times 10^7$	7.5	AGN+EDW <sup>c</sup>
kr37nf	Kroupa	37.5	$256^3$	$3.6 \times 10^7$	7.5	NO FEEDBACK
kr37co-edw500	Kroupa	37.5	$256^3$	$3.6 \times 10^7$	7.5	COUPLED EDW <sup>d</sup>
ay37edw500	Arimoto-Yoshii	37.5	$256^3$	$3.6 \times 10^7$	7.5	EDW
sa37edw500	Salpeter	37.5	$256^3$	$3.6 \times 10^7$	7.5	EDW
kr37p400edw500	Kroupa	37.5	$400^3$	$9.4 \times 10^6$	4.8	EDW

**Table 2.** Summary of the different runs. Column 1, run name; column 2, Initial Mass Function (IMF) chosen; column 3, comoving box size; column 4, number of gas particles; column 5, mass of gas particle; column 6, Plummer-equivalent comoving gravitational softening; column 7, type of feedback implemented. For the runs kr37edw500, kr37co-edw500, ay37edw500, sa37edw500 and kr37p400edw500 the velocity of the energy-driven winds (EDW) is set to  $v_w = 500 \text{ km s}^{-1}$ . (a): momentum-driven winds (MDW) feedback in which wind velocity scales roughly with  $3\sigma$  ( $\sigma$  being the velocity dispersion of the halo that hosts the “wind” particle). (b): AGN feedback in which the energy is released by gas accretion onto super-massive black holes. (c): combined effect of energy-driven winds of  $300 \text{ km s}^{-1}$  and AGN feedbacks. (d): energy-driven winds not decoupled from the hydrodynamics (see Section 3.1).

in the cooling function using the tables of Sutherland & Dopita (1993), that assume the solar value for the relative abundances. In this paper we use the solar metallicity and element abundances given by Asplund et al. (2005), with  $Z/X = 0.0165$ . Besides including different contributions from Type II and Type Ia supernovae (SN II, SN Ia) and Low and Intermediate-Mass Stars (LIMS), our model of chemical evolution accounts for mass-dependent stellar lifetimes. We adopt the lifetime function given by Padovani & Matteucci (1993). For the stellar yields we use: SNIa – Thielemann et al. (2003); SNII – Woosley & Weaver (1995); LIMS – van den Hoek & Groenewegen (1997). The mass-range for the SNII is  $m > 8M_{\odot}$ , while for the SNIa is  $m < 8M_{\odot}$  with a binary fraction of 10%. Finally we use three distinct stellar initial mass functions (IMFs): a Kroupa, a Salpeter and an Arimoto-Yoshii IMF. For this paper our reference choice is the Kroupa IMF (Kroupa 2001), which consists of a multi-slope approximation:  $y_{\text{KR}} = 0.3$  for stellar mass  $m < 0.5M_{\odot}$ ,  $y_{\text{KR}} = 1.2$  for  $0.5M_{\odot} \leq m < 1M_{\odot}$  and  $y_{\text{KR}} = 1.7$  for  $m \geq 1M_{\odot}$  (where  $\varphi(m) \propto m^{-y}$  is the functional form for the IMF and  $\varphi(m)$  is the IMF by mass). Salpeter (Salpeter 1955) IMF has single slope  $y_{\text{SL}} = 1.35$  and Arimoto-Yoshii (Arimoto & Yoshii 1987) IMF also has single slope  $y_{\text{AY}} = 0.95$ .

In this paper we use three different feedback schemes: two associated to the galactic (energy and momentum driven) winds produced by “starburst” galaxies, already presented in Tescari et al. (2009), and the (new) AGN feedback associated to the energy released by gas accretion onto super-massive black holes. In the following we briefly describe these different models.

### 3.1 Energy-driven winds

For this implementation, the wind mass-loss rate  $\dot{M}_w$  is assumed to be proportional to the star formation rate  $\dot{M}_{\star}$  according to

$$\dot{M}_w = \eta \dot{M}_{\star}, \quad (1)$$

where  $\eta$  is the wind mass loading factor (i.e. the wind efficiency), and the wind carries a fixed fraction  $\chi$  of SN energy:

$$\frac{1}{2} \dot{M}_w v_w^2 = \chi \epsilon_{\text{SN}} \dot{M}_{\star}. \quad (2)$$

Star forming gas particles are then stochastically selected according to their star formation rate to become part of a blowing wind. Whenever a particle is uploaded to the wind, it is decoupled from the hydrodynamics for a given period of time or till the density around it drops below a given fraction of the density threshold for the onset of the star formation ( $\rho_{\text{th}} = 0.1 \text{ cm}^{-3}$  in terms of the number density of hydrogen atoms), in order to effectively reach less dense regions. The (lower) limiting density for decoupling is set to  $0.5\rho_{\text{th}}$ . This allows the wind particle to travel “freely” up to few kpc until it has left the dense star forming phase, without directly interacting with it. Otherwise, to verify the effect of the decoupling, we run a “coupled winds” simulation in which wind particles are always affected by the hydrodynamics like all the other gas particles (see also Dalla Vecchia & Schaye 2008; Tornatore et al. 2010). Unlike in Springel & Hernquist (2003), we fixed the velocity of the winds,  $v_w$ , instead of the fraction of the energy made available by SNII explosions to power galactic ejecta. Thus, four parameters fully specify the wind model: the wind efficiency  $\eta$ , the wind speed  $v_w$ , the wind free travel length  $l_w$  and the wind free travel density factor  $\delta_w$ . The maximum allowed time for a wind particle to stay hydrodynamically decoupled is then  $t_{\text{dec}} = l_w/v_w$  (note that in the case of coupled winds  $t_{\text{dec}} = 0$ ). The parameter  $l_w$  has been introduced in order to prevent a gas particle from being trapped into the potential well of the virialized halo and in order to effectively escape from the ISM, reach the low density IGM and pollute it with metals.

In this paper, we use  $l_w = 10 h^{-1} \text{ kpc}$  and we considered two different values for the wind velocity:  $v_w = 300$  and  $500 \text{ km s}^{-1}$ . In our implementation the parameter  $\eta$  is kept fixed to the value 2.

### 3.2 Momentum-driven winds

A feasible physical scenario for the wind driving mechanism, outlined by Murray et al. (2005) to explain observational evidence of outflows from starburst galaxies (Martin 2005; Rupke et al. 2005), is the so called momentum-driven wind model. In this scenario, the radiation pressure of the starburst drives an outflow, possibly by transferring momentum to an absorptive component (e.g. dust) that is hydrodynamically coupled with the gas component, which is then dragged out of the galaxy. Following Oppenheimer & Davé

(2006, 2008) we implemented the momentum-driven winds model in our code. In such a model the wind speed scales as the galaxy velocity dispersion  $\sigma$ , as observed by Martin (2005). Since in momentum-driven winds the amount of input momentum per unit star formation is constant, this implies that the wind mass loading factor  $\eta$  must be inversely proportional to the velocity dispersion. We therefore use the following relations:

$$v_{\text{wind}} = 3\sigma\sqrt{f_L - 1}; \quad \eta = \frac{\sigma_0}{\sigma}, \quad (3)$$

where  $f_L$  is the luminosity factor in units of the galactic Eddington luminosity (i.e. the critical luminosity necessary to expel gas from the galaxy),  $\sigma_0$  is the normalization of the mass loading factor and we add an extra  $2\sigma$  kick to get out of the potential of the galaxy in order to simulate continuous pumping of gas until it is well into the galactic halo. To determine  $\sigma$ , we identify haloes runtime in the simulations by using a parallel friends-of-friends (FoF) algorithm and we associate  $\sigma$  with the velocity dispersion of the haloes,  $\sigma_{\text{DM}}$  (for further details see Section 2.2 of Tesfari et al. 2009). Schaerer (2003) suggested an approximate functional form for far-UV emission which Oppenheimer & Davé (2006, 2008) used to obtain the luminosity factor and which includes a metallicity dependence for  $f_L$ , owing to more UV photons output by lower-metallicity stellar populations:

$$f_L = f_{L,\odot} \times 10^{-0.0029(\log Z+9)^{2.5}+0.417694}, \quad (4)$$

where Martin (2005) suggests:  $f_{L,\odot} \approx 2$ . The mass loading factor controls star formation at early times, so  $\sigma_0$  can also be set by requiring a match to the observed global star formation rate. Following Oppenheimer & Davé (2006, 2008) we set  $\sigma_0 = 150 \text{ km s}^{-1}$ . Even for this wind implementation the particles are stochastically selected in the same way as for the energy-driven scenario.

### 3.3 AGN feedback

Finally, we include in our simulations the effect of feedback energy from gas accretion onto super-massive black holes (BHs), following the scheme originally introduced by Springel et al. (2005) (see also Di Matteo et al. 2005). In this model, BHs are represented by collisionless sink particles initially seeded in dark matter haloes, which subsequently grow via gas accretion and through mergers with other BHs during close encounters. Every new dark matter halo, identified by a run-time friends-of-friends algorithm, above the mass threshold  $M_{\text{th}} = 10^{10} M_{\odot}$ , is seeded with a central BH of initial mass  $10^5 M_{\odot}$ , provided the halo does not contain any BH yet. Each BH can then grow by local gas accretion, with a rate given by

$$\dot{M}_{\text{BH}} = \min(\dot{M}_{\text{B}}, \dot{M}_{\text{Edd}}), \quad (5)$$

where  $\dot{M}_{\text{B}}$  is the accretion rate estimated with the Bondi-Hoyle-Littleton formula (e.g. Bondi 1952) and  $\dot{M}_{\text{Edd}}$  is the Eddington accretion rate. We refer to Springel et al. (2005) for the details of the AGN feedback implementation and to Booth & Schaye (2009) for a review of the black holes accretion feedback in the context of cosmological simulations. An important parameter of the model is the radiative efficiency,  $\epsilon_r$ , which gives the radiated energy  $L_r$  in units of the energy associated to the accreted mass:

$$\epsilon_r = \frac{L_r}{\dot{M}_{\text{BH}}c^2}. \quad (6)$$

Following Springel et al. (2005) and Fabjan et al. (2010), we fix  $\epsilon_r = 0.1$  as a reference value, which is typical for a radiatively

efficient accretion onto a Schwarzschild BH (Shakura & Sunyaev 1973). The model then assumes that a fraction  $\epsilon_f$  of the radiated energy is thermally coupled to the surrounding gas, so that  $\dot{E}_{\text{feed}} = \epsilon_r\epsilon_f\dot{M}_{\text{BH}}c^2$  is the rate of the energy released to heat the surrounding gas. Using  $\epsilon_f \sim 0.05$ , Di Matteo et al. (2005) were able to reproduce the observed  $M_{\text{BH}} - \sigma$  relation between bulge velocity dispersion and mass of the hosted BH (see also Sijacki et al. 2008; Di Matteo et al. 2008). Gas particle accretion onto the BH is implemented in a stochastic way, by assigning to each neighbouring gas particle a probability of contributing to the accretion, which is proportional to the SPH kernel weight computed at the particle position. In the scheme described above, this stochastic accretion is used only to increase the dynamic mass of the BHs, while the mass entering in the computation of the accretion rate is followed in a continuous way, by integrating the analytic expression for  $\dot{M}_{\text{BH}}$ . Once the amount of energy to be thermalized is computed for each BH at a given timestep, this energy is then distributed to the surrounding gas particles using the SPH kernel weighting scheme. Our research group explored for the first time this new feedback prescription in relation to the high redshift properties of the intergalactic medium, while Tornatore et al. (2010) have studied the impact of this feedback mechanism on the low redshift IGM (other groups are working on the black holes accretion feedback related to IGM and the Warm Hot Intergalactic Medium (WHIM), see for example Wiersma et al. 2010; Bertone et al. 2010,?).

In Table 2 we summarize the main parameters of the cosmological simulations performed, including the mass associated to the gas particles and the gravitational softening. All the simulations start at redshift  $z = 99$  and stop at redshift  $z = 1.5$ . In the following we outline the specific characteristics of each run:

- **kr37edw500**: Energy-driven winds (EDW) of velocity  $v_w = 500 \text{ km s}^{-1}$  and Kroupa IMF (the reference IMF for this work).
- **kr37mdw**: Momentum-driven winds (MDW) and Kroupa IMF.
- **kr37agn**: In this simulation the AGN feedback mechanism, associated to the energy released by gas accretion onto super-massive black holes and described in Section 3.3, is active.
- **kr37agn+edw300**: In this simulation two different feedback models are combined: the energy-driven galactic winds of velocity  $v_w = 300 \text{ km s}^{-1}$ , and the AGN feedback. We will see that this run is completely different from the kr37agn simulation mentioned above. In fact, the galactic winds start to be effective at higher redshift than the AGN feedback, making the haloes devoid of gas and consequently reducing the efficiency of the black holes accretion and the power of the AGN feedback. Therefore, the effect of the winds is more prominent than that of the AGN, with the result that the kr37agn+edw300 run behaves very similarly to a regular energy-driven winds simulation.
- **kr37nf**: This simulation was run without any winds or AGN feedback in order to test how large the effects of the different feedback prescriptions on the CIV statistics are.
- **kr37co-edw500**: as we stated in Section 3.1, this simulation has energy-driven winds of velocity  $v_w = 500 \text{ km s}^{-1}$ , never decoupled from the hydrodynamics. We will show that the coupled winds result in a less efficient feedback with respect to the original implementation.
- **ay37edw500**: Energy-driven winds of velocity  $v_w = 500 \text{ km s}^{-1}$  and Arimoto-Yoshii IMF.
- **sa37edw500**: Energy-driven winds of velocity  $v_w = 500$

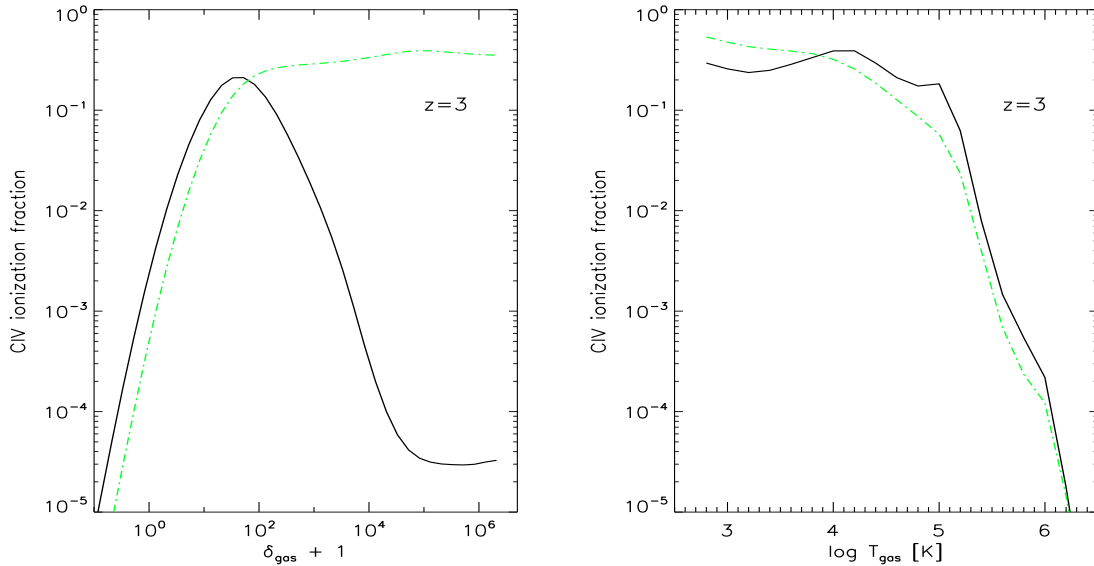


**Figure 1.** *Left panel:* CIV ionization fraction, as a function of the gas overdensity, at  $z = 3$  for a gas temperature of  $10^{4.6}$  K (solid black line) and  $10^{5.0}$  K (dot-dashed green line). *Right panel:* CIV ionization fraction, as a function of the gas temperature, at  $z = 3$  for an overdensity of  $\delta_{\text{gas}} \sim 50$  (solid black line) and  $\delta_{\text{gas}} \sim 10$  (dot-dashed green line).

$\text{km s}^{-1}$  and Salpeter IMF (runs kr37edw500, ay37edw500 and sa37edw500 are identical except for the IMF).

- **kr37p400edw500:** Energy-driven winds of velocity  $v_w = 500 \text{ km s}^{-1}$  and Kroupa IMF, with a number of particles (gas + dark matter) equal to  $2 \times 400^3$ . This simulation is identical to the kr37edw500 except for the larger number of particles and was run in order to check for resolution effects.

The name of each simulation reflects the choice of the IMF, the box size (even if the box size is equal to  $37.5 h^{-1}$  Mpc for all the simulations, we report it in order to be consistent with other works, e.g. Oppenheimer & Davé 2006, 2008) and the feedback prescription adopted (only in the case of the resolution test run, kr37p400edw500, the number of particles is specified in the name). In this paper, we label as “reference runs” the first three of the list above: kr37edw500, kr37mdw and kr37agn.

We use the CLOUDY code (Ferland et al. 1998) to compute a-posteriori the CIV ionization fractions for each gas particle. As for the work presented in Tescari et al. (2009), we choose the HM05 option in CLOUDY, which consists of a UVB made by QSOs and galaxies with a 10% photon escape fraction and which is in agreement with other observational constraints (Bolton et al. 2005). In the left panel of Figure 1 we plot the CIV ionization fraction, as a function of the gas overdensity  $\delta_{\text{gas}} + 1 = \rho_{\text{gas}}/\bar{\rho}$ , at  $z = 3$  for a gas temperature of  $10^{4.6}$  K (solid black line) and  $10^{5.0}$  K (dot-dashed green line). In the right panel we plot the same ionization fraction, as a function of the gas temperature  $T_{\text{gas}}$ , at  $z = 3$  for an overdensity of  $\delta_{\text{gas}} \sim 50$  (solid black line), this value being representative of the outskirts of dark matter haloes, and  $\delta_{\text{gas}} \sim 10$  (dot-dashed green line).

#### 4 STAR FORMATION RATES AND EVOLUTION OF THE TOTAL CIV CONTENT

In this Section we analyse the cosmic star formation rates (SFRs) and the evolution of the total Carbon content in the different simulations.

In the left panel of Figure 2 we report the total SFR of the simulated volume as a function of redshift. All the simulations, except the kr37p400edw500 run, have the same SFR down to redshift  $z \sim 9.5$ , when they start to differ due to their distinct feedback recipes. Run kr37nf (no-feedback, green dots) has the highest star formation rate compared to the other runs because there is no effective mechanism able to quench the star formation. Run kr37agn (AGN-feedback, black dots) follows the no-feedback run kr37nf down to redshift  $z = 3$ , but then the AGN feedback becomes effective and the SFR suddenly decreases. Runs kr37co-edw500 (coupled energy-driven winds, red dots), kr37edw500 (energy-driven winds, cyan dots) and kr37mdw (momentum-driven winds, blue dots) show more or less the same trend but for the kr37co-edw500 the SFR is slightly higher due to the fact that the coupled winds are less efficient than the normal winds in making the central region of the haloes devoid of gas and therefore in suppressing the star formation. The kr37agn+edw300 simulation (AGN + energy-driven winds, yellow dots) follows the other “wind” runs (kr37co-edw500, kr37edw500 and kr37mdw) until redshift  $z = 3$  but then the AGN feedback starts to become active and suppresses the star formation very efficiently. Finally, at  $z > 8$ , the kr37p400edw500 run (resolution test, grey dots), shows a higher star formation with respect to the other runs due to the improved resolution of this simulation that can resolve higher densities at earlier times. Going to lower redshift the SFR of the kr37p400edw500 agrees very well with that of the kr37edw500 run, which has the same boxsize and parameters but poorer resolution. This confirms the numerical convergence of our simulations in the regime we are interested in. We stress that the aim of this plot is to underline the effect of the different feedback prescriptions on the SFR. For this reason observational data

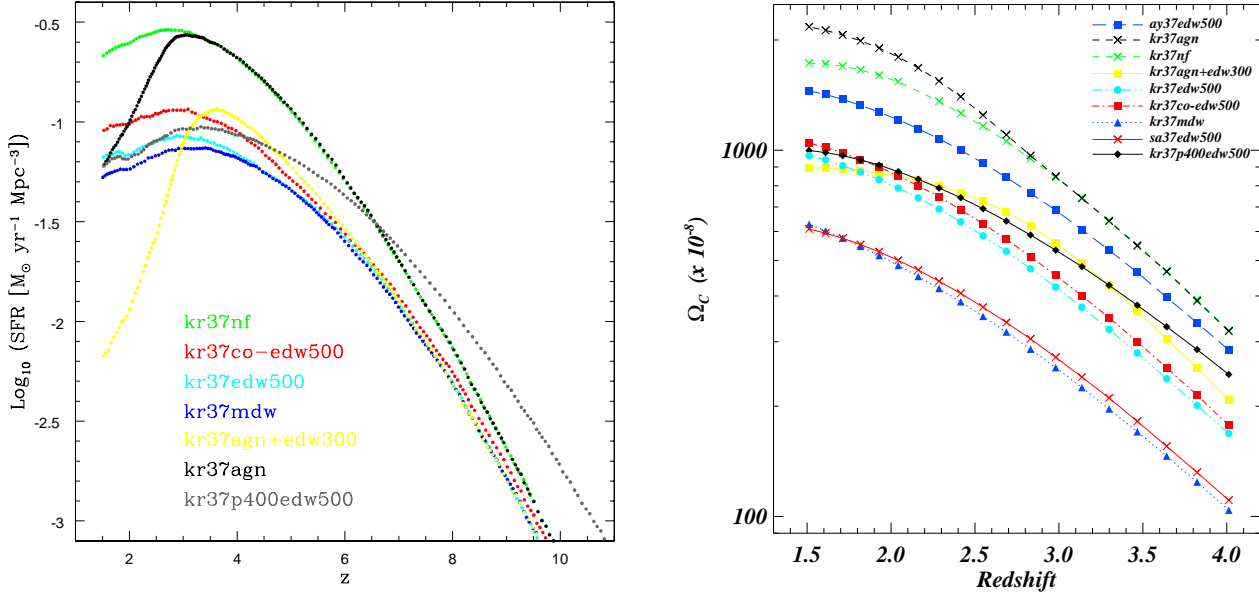


**Figure 2.** *Left Panel:* cosmic star formation rate (SFR) for some of the hydrodynamic simulations of Table 2. *Right Panel:* evolution of the total  $\Omega_C$  as a function of redshift for all the hydrodynamic simulations of Table 2.

are not plotted, because our simulations can be tuned in order to fit the observed cosmic star formation rate at low redshift and, in this sense, kr37edw500 is the reference simulation: all the other runs in this plot differ only for the feedback prescription (all of them have Kroupa IMF) and were not re-tuned. We also did not plot the two runs with different IMFs ay37edw500 (Arimoto-Yoshii IMF) and sa37edw500 (Salpeter IMF), because we do not change the star formation efficiency as it would be required in order to match the observables when the number of massive stars per unit mass of formed stars changes: we are more interested in the chemical and energetic effect of the IMF.

In the right panel of Figure 2 we show the evolution with redshift of the Carbon cosmological mass density  $\Omega_C(z)$ , calculated considering the sum of the Carbon content associated to each particle inside the cosmological box. Energy-driven winds runs kr37edw500 (cyan circles—triple-dot-dashed line), ay37edw500 (blue squares—dashed line) and sa37edw500 (red crosses—solid line) are identical except for the IMF, therefore the comparison of these three simulations is useful to understand how Carbon production is affected by the choice of the IMF. The evolution of  $\Omega_C$  is in fact the same, but with different normalization: ay37edw500 has Arimoto-Yoshii IMF and produces more Carbon than kr37edw500 run (Kroupa IMF) which itself produces more Carbon than sa37edw500 (Salpeter IMF). With the Kroupa IMF, the relative fraction of intermediate-mass stars, i.e. stars with masses  $2M_{\odot} \leq m \leq 8M_{\odot}$ , representing important Carbon producers, is larger than with the Salpeter IMF (Calura & Matteucci 2006; Calura & Menci 2009). For this reason,  $\Omega_C$  obtained with the Kroupa IMF is higher than that obtained with the Salpeter IMF. On the other hand, the assumption of a top-heavy IMF, such as the one of Arimoto & Yoshii (1987), strongly enhances the number of massive stars but suppresses the fraction of intermediate mass stars, with the overall result of a higher Carbon density at any cosmic epoch. Interestingly, run kr37mdw (momentum-driven winds, blue triangles—dotted line) follows the sa37edw500 even if the latter

produces much less CIV as we will show in Section 7 (Figure 12, left panel). Run kr37co-edw500 (coupled energy-driven winds, red squares—dot-dashed line) has the same trend as kr37edw500 but with a slightly higher normalization. As we stated above, this is due to the fact that the coupled winds are less efficient than the normal winds and therefore this simulation has a higher star formation that results in a higher Carbon abundance. This situation is even more extreme for the kr37nf (no-feedback, green crosses—dashed line) and kr37agn (AGN-feedback, black crosses—dashed line) runs, in fact down to redshift  $z \sim 3$  both of these simulations do not suppress effectively the star formation and for them  $\Omega_C$  is higher. Going to lower redshift AGN feedback becomes active in quenching the star formation and lowers the amount of gas used by the stars and converts in other species (note the excess in  $\Omega_C$  with respect to the kr37nf run at  $z < 2.7$ ). The kr37agn+edw300 run (AGN + energy-driven winds, yellow squares—solid line) shows the same  $\Omega_C$  trend of kr37edw500 even if with higher normalization at high redshift due to the lower strength of the winds ( $300 \text{ km s}^{-1}$  instead of  $500 \text{ km s}^{-1}$ ). At low redshift AGN feedback becomes active, but, differently from the kr37agn case: *i*) winds have already made the haloes devoid of gas therefore reducing the efficiency of the black holes accretion and thus the power of the AGN feedback; *ii*) winds suppress star formation at high redshift lowering the Carbon content, so when the AGN starts to work the net result is a further decrease of  $\Omega_C$ . Finally, at high redshift the kr37p400edw500 run (resolution test, black diamonds—solid line), shows a higher  $\Omega_C$  with respect to the kr37edw500 due to the improved resolution of this simulation (as explained above), while at low redshift the Carbon content of the kr37p400edw500 approaches that of the kr37edw500 run.

Comparing the  $\Omega_C$  evolution of our simulations with the one showed in Oppenheimer & Davé (2006, Figure 12), we found that in general the normalization of our runs is higher, although a very precise comparison is not possible given the different setup of the simulations used, especially regarding the chemical evo-

lution model. However, for the kr37mdw run (and also for the sa37edw500 run) the agreement is much better, the latter simulation producing momentum-driven galactic winds and therefore being the yardstick for the comparison with the Oppenheimer & Davé (2006) work.

## 5 STATISTICS OF HI

Before focusing on the CIV evolution, we address some flux statistics related to the properties and the evolution of neutral hydrogen in the IGM. For all the neutral hydrogen statistics discussed in this paper, we considered HI *lines* (while for the CIV we considered from time to time lines or systems of lines).

For each simulation performed we have extracted several physical quantities interpolated along lines-of-sight (LOSs) through the box. Given the positions, velocities, densities and temperatures of all SPH particles at a given redshift, we compute spectra along a given LOS through the box following the procedure of Theuns et al. (1998). We divide the sight line into  $N = 1024$  bins of width  $\Delta$  in distance  $x$  along the sight line. For a bin  $i$  at position  $x(i)$  we compute the density and the density weighted temperature and velocity from:

$$\rho_X(j) = a^3 \sum_i X(i) \mathcal{W}_{ij}, \quad (7)$$

$$(\rho T)_X(j) = a^3 \sum_i X(i) T(i) \mathcal{W}_{ij}, \quad (8)$$

$$(\rho v)_X(j) = a^3 \sum_i X(i) \{a\dot{x}(i) + \dot{a}[x(i) - x(j)]\} \mathcal{W}_{ij}, \quad (9)$$

where  $a$  is the scale factor,  $X(i)$  is the abundance of species  $X$  of SPH particle  $i$ , assuming ionization equilibrium, and  $\mathcal{W}_{ij} = mW(q_{ij})/h_{ij}^3$  is the normalized SPH kernel. Here  $W$  is the SPH kernel,  $m$  is the SPH particle mass and:

$$q_{ij} = \frac{a|x(i) - x(j)|}{h_{ij}}, \quad (10)$$

$$h_{ij} = \frac{1}{2} [h(i) + h(j)], \quad (11)$$

with  $h$  the physical softening scale. The optical depths of the simulated QSO spectra are drawn in redshift space taking into account the effect of the IGM peculiar velocities along the line-of-sight,  $v_{\text{pec},\parallel}$ .

Taking the case of HI, even if the neutral hydrogen fraction  $f_{\text{HI}}$  is associated to each gas particle and is stored in each simulation snapshot, we follow Nagamine et al. (2004), as in Tescari et al. (2009), to assign a-posteriori a new mass in neutral hydrogen to gas particles above the density threshold for the onset of the star formation (set to  $\rho_{\text{th}} = 0.1 \text{ cm}^{-3}$  in terms of the number density of hydrogen atoms) which reads:

$$m_{\text{HI}} = f_{\text{HI}} m_{\text{H}} \quad (\rho < \rho_{\text{th}}) \quad (12)$$

$$m_{\text{HI}} = f_c m_{\text{H}} \quad (\rho \geq \rho_{\text{th}}), \quad (13)$$

with  $f_{\text{HI}}$  the neutral hydrogen fraction that depends on the UVB used,  $m_{\text{H}}$  the hydrogen mass of the particle ( $f_{\text{HI}}$  and  $m_{\text{H}}$  are determined self-consistently inside the code),  $f_c$  the fraction of mass in cold clouds and  $\rho_{\text{th}}$  the star formation threshold. Here  $f_c = \rho_c/\rho$ , where  $\rho_c$  is the density of cold clouds and  $\rho$  the total (hot + cold) gas density. Individual molecular clouds cannot be resolved at the resolution reachable in cosmological simulations, thus  $\rho_c$  represents an average value computed over small regions of the ISM (Springel & Hernquist 2003).

Our code follows self-consistently the evolution of Carbon (and of other elements, see Section 3), then, using the CLOUDY code (Ferland et al. 1998), we determine the ionization fractions for the CIV ( $\lambda\lambda 1548.204, 1550.781 \text{ \AA}$ ). The simulated flux of a given ion transition at the redshift-space coordinate  $u$  (in  $\text{km s}^{-1}$ ) is  $F(u) = \exp[-\tau(u)]$  with:

$$\tau(u) = \frac{\sigma_{0,\text{I}} c}{H(z)} \int_{-\infty}^{\infty} n_{\text{I}}(x) \mathcal{V} \left[ u - x - v_{\text{pec},\parallel}^{\text{IGM}}(x), b(x) \right] dx, \quad (14)$$

where  $n_{\text{I}}$  is the ion number density,  $\sigma_{0,\text{I}}$  is the cross-section of the particular ion transition,  $H(z)$  is the Hubble constant at redshift  $z$ ,  $x$  is the real-space coordinate (in  $\text{km s}^{-1}$ ),  $b = (2k_{\text{B}}T/m_{\text{I}}c^2)^{1/2}$  is the velocity dispersion in units of  $c$ ,  $\mathcal{V}$  is the Voigt profile. These spectra can be converted from velocity  $v$  to observed wavelength  $\lambda$  using  $\lambda = \lambda_0(1+z)(1+v/c)$ .

After having extracted the spectra along random LOS through the cosmological box for a given simulation at a given redshift  $z$ , we rescaled all the HI optical depths by a constant factor  $A_{\text{HI}}$  (ranging from  $\sim 0.43$  to  $\sim 0.73$ , depending on redshift), in such a way that their mean value was equal to the HI effective optical depth,  $\tau_{\text{HI}}^{\text{eff}}$ , at that redshift, given by the Kim et al. (2007) fitting formula:

$$\tau_{\text{HI}}^{\text{eff}} = (0.0023 \pm 0.0007)(1+z)^{3.65 \pm 0.21}. \quad (15)$$

This rescaling ensures that our spectra match the observed mean normalized flux of the Lyman- $\alpha$  forest at the appropriate redshift:  $\langle F \rangle_{\text{HI,obs}} = \exp(-\tau_{\text{HI}}^{\text{eff}})$ . We also rescaled all the CIV optical depths for the same constant factor  $A_{\text{HI}}$ . Then we convolved the spectra with a Gaussian of  $6.6 \text{ km s}^{-1}$  Full Width at Half-Maximum (FWHM) and we add noise in order to have realistic spectra with signal-to-noise ratio  $S/N = 50$ , to compare with observations. Finally, we run the VPFIT code to fit each spectra and recover HI and CIV lines' redshift, column density and Doppler parameter. Among the lines fitted by VPFIT we have considered only those with relative errors in the Doppler parameter lower than 50%.

### 5.1 The HI column density distribution function

In this Section we compute the Lyman- $\alpha$  forest column density distribution function (HI CDDF)  $d^2n/dNdz$ , namely the number of absorbers with HI column density in the range  $[N, N + dN]$  and redshift path in the interval  $[z, z + dz]$ . The redshift path at a given redshift  $z$  in simulated spectra is given by:

$$dz = n_{\text{spec}}(1+z) \frac{\Delta v}{c}, \quad (16)$$

where  $c$  is the speed of light (in  $\text{km s}^{-1}$ ) and  $n_{\text{spec}}$  is the number of spectra taken at  $z$  for a simulation with box size in  $\text{km s}^{-1}$  equal to  $\Delta v$ .

In Figure 3 we show the HI CDDF at redshift  $z = 3$  for all the simulations of Table 2 splitted in two groups for the sake of clarity. All the simulations fit very well the observational data by D'Odorico et al. (2008) down to column density  $\log N_{\text{HI}} (\text{cm}^{-2}) = 12.2$  and are all in agreement confirming the fact that the HI column density distribution function is quite insensitive to the different feedback prescriptions. Even though the galaxies drive strong winds or AGN feedbacks, there is no discernible effect on the Lyman- $\alpha$  forest. This is due to the fact that winds or black hole ejecta expand preferentially into the lower density regions and so keep the filaments that produce the hydrogen lines intact (Theuns et al. 2002). The volume filling factor of the winds is thus quite small and does not impact strongly on Lyman- $\alpha$  lines. In Figure 4 we show the HI CDDF at redshift  $z = 2.25$ : all



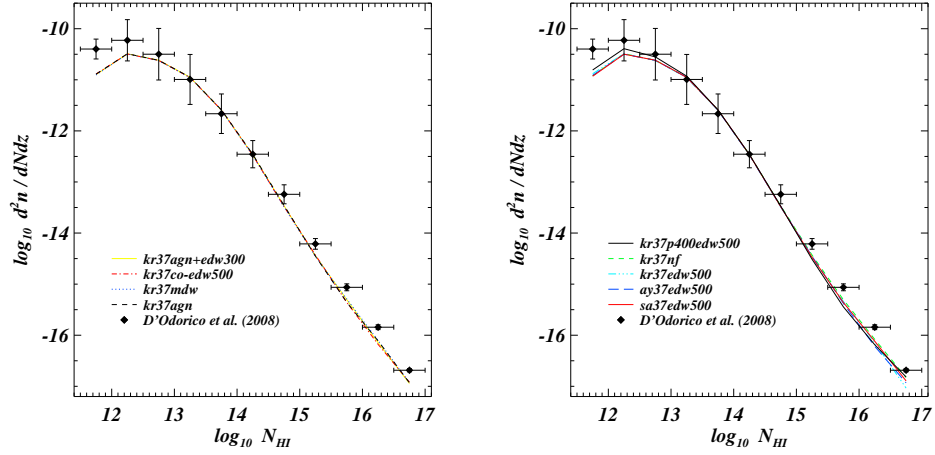


**Figure 3.** Neutral Hydrogen (HI) column density distribution function at  $z = 3$ . *Left panel:* part I (first set of simulations). *Right panel:* part II (second set of simulations). Data from D'Odorico et al. (2008).

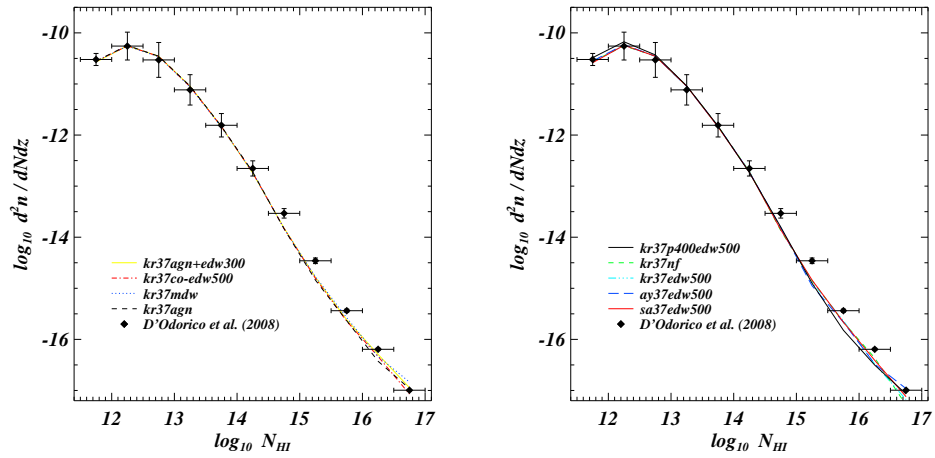


**Figure 4.** As in Figure 3, but at redshift  $z = 2.25$ .

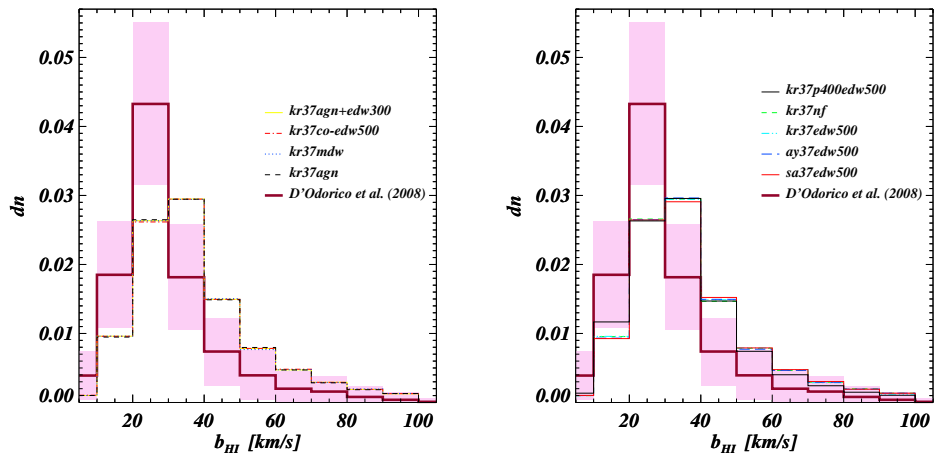


**Figure 5.** Line-widths  $b_{\text{HI}}$  probability distribution function at  $z = 3$ . *Left panel:* part I. *Right panel:* part II. In both panels, data from D'Odorico et al. (2008) are shown by the purple solid line along with the associated Poissonian error (shaded region).

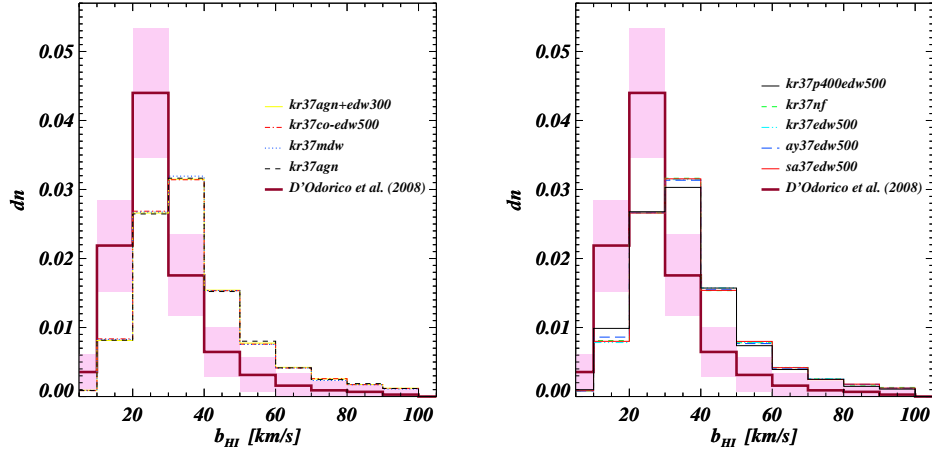


Figure 6. As in Figure 5, but at redshift  $z = 2.25$ .

the previous trends are confirmed and the agreement to the data is very good also for  $\log N_{\text{HI}} (\text{cm}^{-2}) < 12$ .

## 5.2 Probability distribution function of the HI Doppler parameter

In this Section we analyse the Lyman- $\alpha$  Doppler parameter,  $b_{\text{HI}}$ , probability distribution function. Throughout the rest of the paper, both the HI and the CIV Doppler parameters are assumed to be due only to the thermal width of the line and we neglected possible turbulent contribution. Therefore, omitting the turbulent contribution, the Doppler parameter basically measures the temperature of the gas and is defined as:

$$b_{\text{HI}} = \sqrt{\frac{2k_{\text{B}}T}{m_{\text{HI}}}}, \quad (17)$$

where  $m_{\text{HI}}$  is the neutral hydrogen particle mass and  $k_{\text{B}}$  is the Boltzmann's constant. In Figures 5 and 6 we show the Lyman- $\alpha$  Doppler parameter distribution function at redshifts  $z = 3$  and  $z = 2.25$ , respectively, for all the simulations of Table 2, splitted in two groups and compared with the data by D'Odorico et al. (2008) (purple solid line, while the shaded region represents the  $1-\sigma$  Poissonian error). All runs are in good agreement with each other, while they are shifted towards higher  $b_{\text{HI}}$  values with respect to the observational data. At redshift  $z = 3$ , the median value of the observational Doppler parameters distribution is  $25.9 \text{ km s}^{-1}$ , while all the simulations have median around  $\sim 34.5 \text{ km s}^{-1}$ . At  $z = 2.25$ , the data by D'Odorico et al. (2008) have median value equal to  $24.8 \text{ km s}^{-1}$ , while the simulations have median around  $\sim 34.9 \text{ km s}^{-1}$ .

Our simulations produce HI gas that is too hot compared to the observations. There can be many reasons for this, both physical and numerical. Regarding the former, it is very important to stress the effect of the UV background on the gas: if the UV background is too strong the gas will be heated too much. As stated in Section 3, we multiplied the Haardt & Madau (1996) heating rates by a factor of 3.3, introduced to fit the Schaye et al. (2000b) constraints on the temperature evolution of the intergalactic medium. It seems that this correction does not work properly with new and higher quality data sets.

However, minor part of the discrepancy is due to the lines fitting procedure. When the absorption lines are weak and not well

defined, VPFIT can add relatively broad components in order to minimize the  $\chi^2$  statistics. This spurious components could have large equivalent width and low optical depth, therefore they have negligible impact on the column density distribution function because of their relative small column density, but they can bias the Doppler parameter probability distribution function. We will show later in Section 9 that this numerical effect is more evident for the CIV statistics and how it is important in explaining some features of the  $b_{\text{CIV}} - N_{\text{CIV}}$  relation.

## 5.3 Column density-Doppler parameter relation

In Figures 7 and 8 we plot the  $b_{\text{HI}} - N_{\text{HI}}$  relation, at redshift  $z = 3$  and  $z = 2.25$  respectively, for the reference simulations kr37edw500, kr37mdw and kr37agn. The contour plots are colour coded according to the fraction of points that fall in each bin with coordinate  $(b_{\text{HI}}, N_{\text{HI}})$ . In the upper left panels the observational data of D'Odorico et al. (2008) are reported. Both at redshifts  $z = 3$  and  $z = 2.25$  all runs are in good agreement with each other and reproduce well the observations, even if the simulations present Doppler parameters slightly higher than the observational data (as we mentioned in the previous Section). The mean slope of the data envelope in the column density range  $11.5 < \log N_{\text{HI}} (\text{cm}^{-2}) < 15$  measures the slope of the  $T - \rho$  relation for the gas (Schaye 2001), and all the runs show roughly the same right slope of the data at the two redshifts.

To sum up, the fact that for our simulations all the different HI statistics are in general agreement with the observational data, confirms that we are catching the physics of the gas traced by the neutral hydrogen. The discrepancies are due, mainly, to the choice of the UV background (assumed to be produced by quasars and galaxies as given by Haardt & Madau 1996, with the heating rates multiplied by a factor of 3.3, see Sections 3 and 5.2) and, in minor part, to a numerical effect introduced by VPFIT that affects our analysis of the absorption lines in quasar spectra. We will discuss in more detail the impact of this effect in the next sessions regarding the CIV absorption lines statistics.

The resolution-test simulation kr37p400edw500 follows the other runs in all the previous statistics, again confirming the numerical convergence of our simulations for the HI evolution.

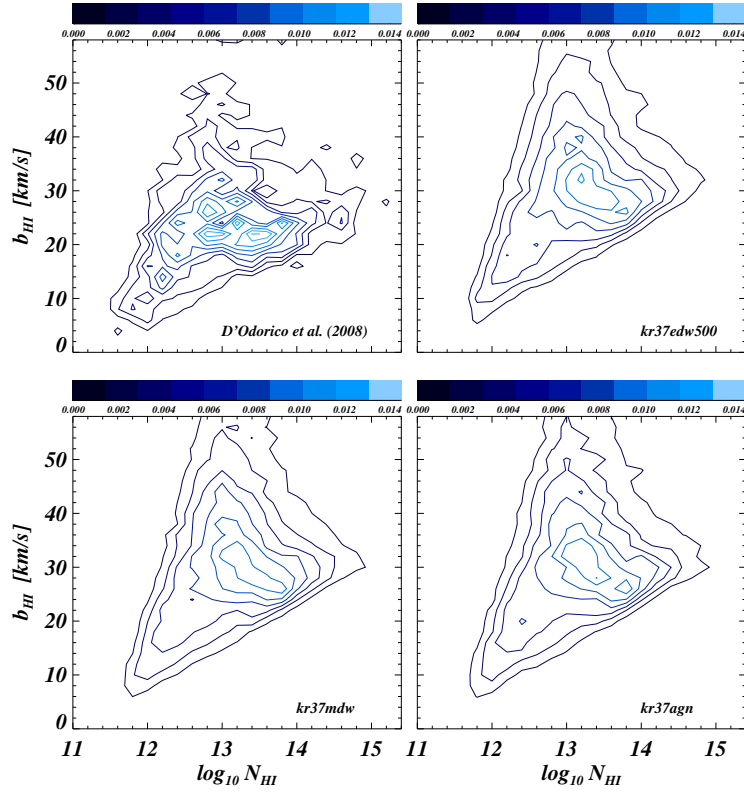


**Figure 7.**  $b_{\text{HI}} - N_{\text{HI}}$  relation at  $z = 3$ . The horizontal bars are colour coded according to the fraction of points that fall in each bin with coordinate  $(b_{\text{HI}}, N_{\text{HI}})$ . Upper left panel: observational data from D'Odorico et al. (2008).

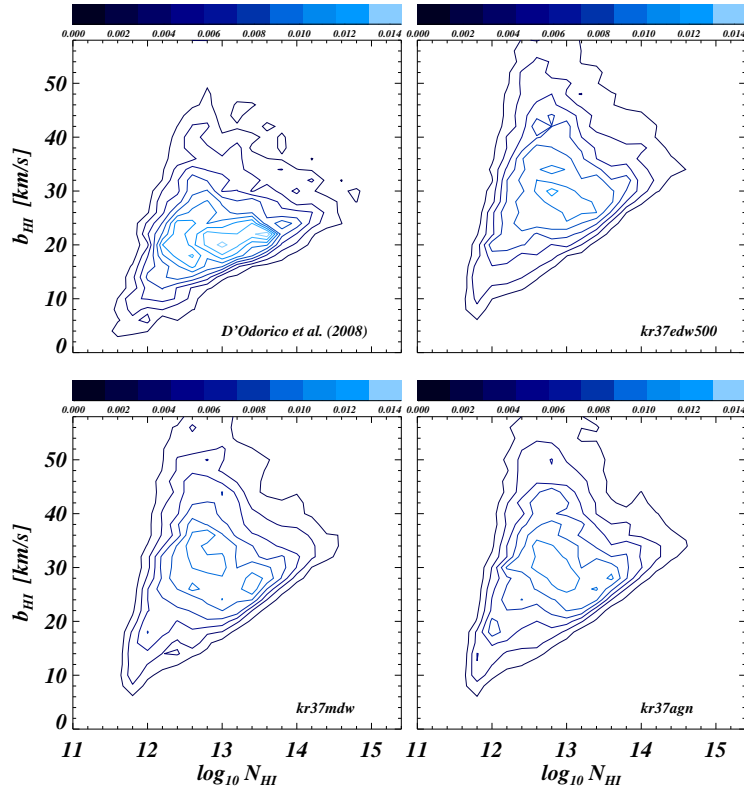


**Figure 8.** As in Figure 7, but at redshift  $z = 2.25$ .

## 6 THE CIV COLUMN DENSITY DISTRIBUTION FUNCTION

In this Section we investigate the CIV column density distribution function (CIV CDDF, already defined in Section 5.1), plotted at redshift  $z = 3, 2.25$  and  $1.5$ , respectively and along with the D’Odorico et al. (2010) data, in Figures 9, 10 and 11. We considered for this analysis *systems* of lines as defined in Section 2.

At  $z = 3$  (Figure 9), runs (left panel) kr37agn+edw300 (AGN + energy-driven winds), kr37co-edw500 (coupled energy-driven winds), kr37mdw (momentum-driven winds) and (right panel) kr37edw500 (energy-driven winds, Kroupa IMF), ay37edw500 (energy-driven winds, Arimoto-Yoshii IMF), sa37edw500 (energy-driven winds, Salpeter IMF), are in agreement with each other and reproduce well the observed distribution down to  $\log N_{\text{CIV}} (\text{cm}^{-2}) \sim 12.7$ . In contrast, for the simulations kr37nf and kr37agn the agreement is not good. Simulation kr37nf (Figure 9 right panel, green dashed line) was run, as a test, without any winds or AGN feedback: so there is no effective mechanism to spread the enriched gas outside the haloes. The result is that all the gas is trapped inside high density haloes and most of the Carbon is locked back into stars. In the run kr37agn (Figure 9 left panel, black dashed line) the feedback mechanism is the AGN feedback, associated to the energy released by gas accretion onto supermassive black holes. Comparing the resulting distribution with that of kr37nf, we note that they are very similar. The reason is that at redshift  $z = 3$  the AGN feedback is not active yet, but it is just starting to work, so at high redshift this simulation virtually behaves like the no-feedback one. Interestingly, run kr37agn+edw300 (AGN + energy-driven winds) follows all the other “wind” runs even if in this case we have the combined effect of winds and AGN feedbacks: this is due to the fact that winds start to be effective at higher redshift than the AGN feedback, making the haloes devoid of gas and in this way reducing the efficiency of the black holes accretion and the power of the AGN feedback.

At redshift  $z = 2.25$  (Figure 10), the agreement with observational data is very good down to  $\log N_{\text{CIV}} (\text{cm}^{-2}) = 12$ . The kr37nf run (no-feedback, right panel dashed green line) suffers of the same problems described before, while for the kr37agn run (AGN feedback, left panel dashed black line) the discrepancies with the observational data decreased: a first hint that going to lower redshift AGN feedback becomes more and more efficient and the behaviour of this simulation starts to resemble that of the “wind” runs.

At redshift  $z = 1.5$  (Figure 11) all the simulations produce too many systems with low column density and systematically fall slightly short of reproducing the distribution at  $\log N_{\text{CIV}} (\text{cm}^{-2}) > 14.5$ . Now the kr37agn run (AGN feedback, left panel dashed black line) closely follows all the other runs, confirming that at this low redshift AGN feedback is active and powerful, while kr37nf run (no feedback, right panel dashed green line) still fails in reproducing the correct trend. For this statistics, at the three redshift considered, the resolution-test simulation kr37p400edw500 follows the reference runs.

Note that at redshift  $z = 2.25$  we fit very well the observational data in the low column density tail of the distribution,  $\log N_{\text{CIV}} (\text{cm}^{-2}) < 12.2$ , while at  $z = 3$  and  $z = 1.5$  the agreement in this column density range gets worse.

## 7 THE EVOLUTION OF THE CIV COSMOLOGICAL MASS DENSITY

In the left panel of Figure 12 we show  $\Omega_{\text{CIV}}(z)$ , calculated considering the sum of the CIV content associated to each particle inside the cosmological box. Energy-driven winds runs kr37edw500 (cyan circles–triple dot-dashed line), ay37edw500 (blue squares–dashed line) and sa37edw500 (red crosses–solid line) behave exactly as we described in Section 4: they differ only for the IMF and the ay37edw500 produces much more CIV than the other two, having Arimoto-Yoshii IMF. Runs kr37co-edw500 (coupled energy-driven winds, red squares–dot-dashed line) and kr37mdw (momentum-driven winds, blue triangles–dotted line) follow almost the same trend as kr37edw500, which has the same IMF of the two runs mentioned above. For the kr37nf simulation (no-feedback, green crosses–dashed line),  $\Omega_{\text{CIV}}$  starts to decrease at redshift  $z \sim 2.7$ . It is interesting to note that for the simulation kr37agn (AGN-feedback, black crosses–dashed line)  $\Omega_{\text{CIV}}$  suddenly increases after a small decrement at redshift  $z \sim 2.8$  (down to this redshift the kr37agn run follows the no-feedback run). This is due to the suppression of star formation produced by the powerful AGN feedback. Then, moving to lower redshift the CIV cosmological density starts to approach all the other runs. The same effect is visible in the kr37agn+edw300 run (AGN + energy-driven winds, yellow squares–solid line). In this case the effect is weaker because, as we explained in Section 6, winds make the haloes devoid of gas therefore reducing the efficiency of the black holes accretion and thus the power of the AGN feedback. As for the total  $\Omega_{\text{C}}$  plot in the right panel of Figure 2, at high redshift, the resolution-test simulation kr37p400edw500, shows a higher  $\Omega_{\text{CIV}}$  with respect to the kr37edw500, while the two runs are in agreement at low redshift.

In the right panel of Figure 12 we show the evolution with redshift of the CIV cosmological mass density as a fraction of the critical density today, calculated considering the column density distribution function of the CIV absorption lines:

$$\Omega_{\text{CIV}}(z) = \frac{H_0 m_{\text{CIV}}}{c \rho_{\text{crit}}} \int N f(N) dN, \quad (18)$$

where  $H_0 = 100 h \text{ km s}^{-1} \text{ Mpc}^{-1}$  is the Hubble constant ( $h = 0.73$ ),  $m_{\text{CIV}}$  is the mass of a CIV ion,  $c$  is the speed of light,  $\rho_{\text{crit}} = 1.88 \times 10^{-29} h^2 \text{ g cm}^{-3}$  and  $f(N)$  is the CIV CDDF. Since  $f(N)$  cannot be recovered correctly for all the column densities due to incompleteness and poor statistics, the integral in the previous equation can be approximated by a sum (Storrie-Lombardi et al. 1996):

$$\Omega_{\text{CIV}}(z) = \frac{H_0 m_{\text{CIV}} \sum_i N_i(\text{CIV})}{c \rho_{\text{crit}} \Delta X}, \quad (19)$$

with  $\Delta X \equiv \int (1+z)^2 [\Omega_{\text{0m}}(1+z)^3 + \Omega_{\text{0}\Lambda}]^{-1/2} dz$ , the redshift absorption path. In the right panel of Figure 12 the overplotted black diamonds show the observational data of D’Odorico et al. (2010). The value of  $\Omega_{\text{CIV}}$  significantly depends on the column density range over which the sum or the integration is carried out and, as a consequence, on the resolution and signal-to-noise ratio of the available spectra. In order to address this aspect, D’Odorico et al. (2010) have computed three sets of values to be compared consistently with different data in the literature. Here we compared  $\Omega_{\text{CIV}}$  obtained from the simulated CIV *systems* (as defined in Section 2) lying in the column density range  $12 \leq \log N_{\text{CIV}} (\text{cm}^{-2}) \leq 15$ , with the  $\Omega_{\text{CIV}}$  computed from the CIV systems of the total D’Odorico et al. (2010) sample, in the same

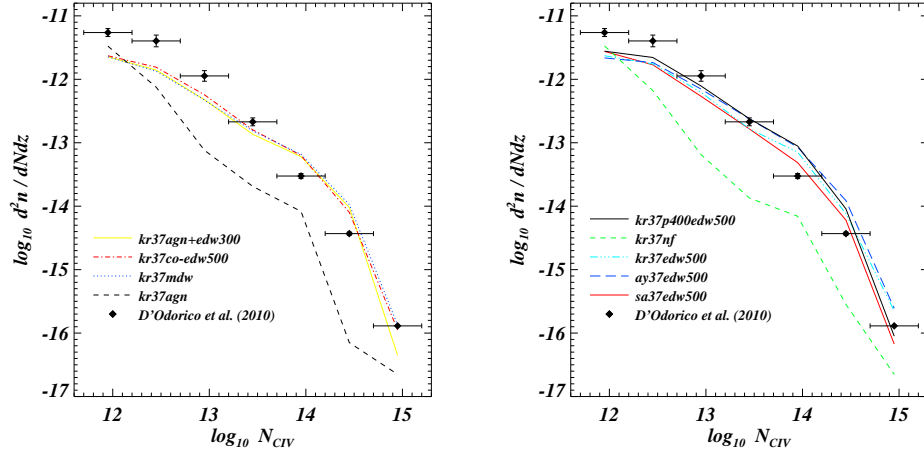


Figure 9. CIV column density distribution function at  $z = 3$ . *Left panel*: part I. *Right panel*: part II. Data from D'Odorico et al. (2010).

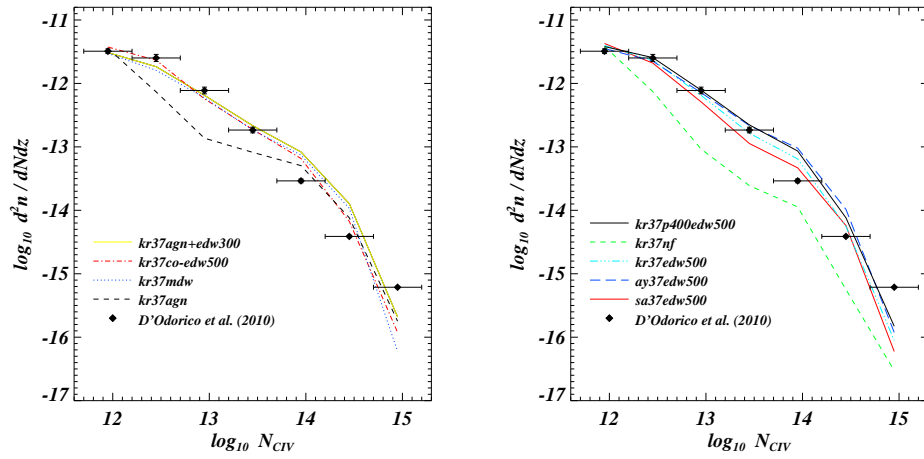


Figure 10. As in Figure 9, but at redshift  $z = 2.25$ .

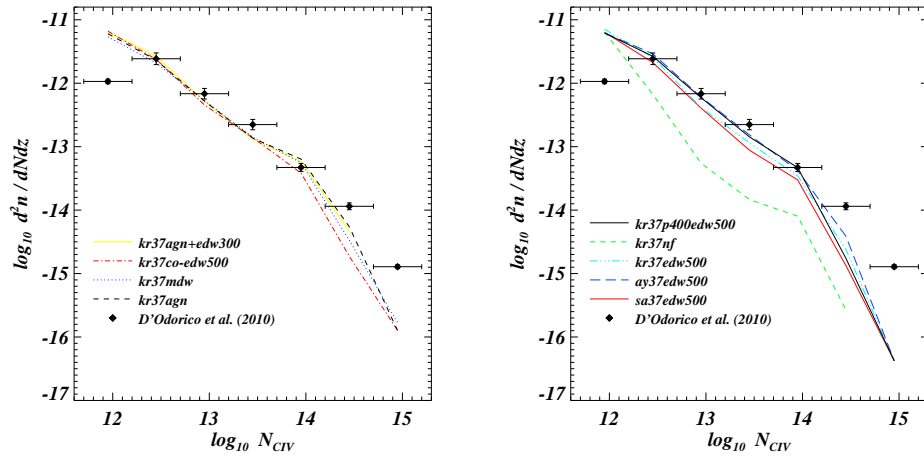
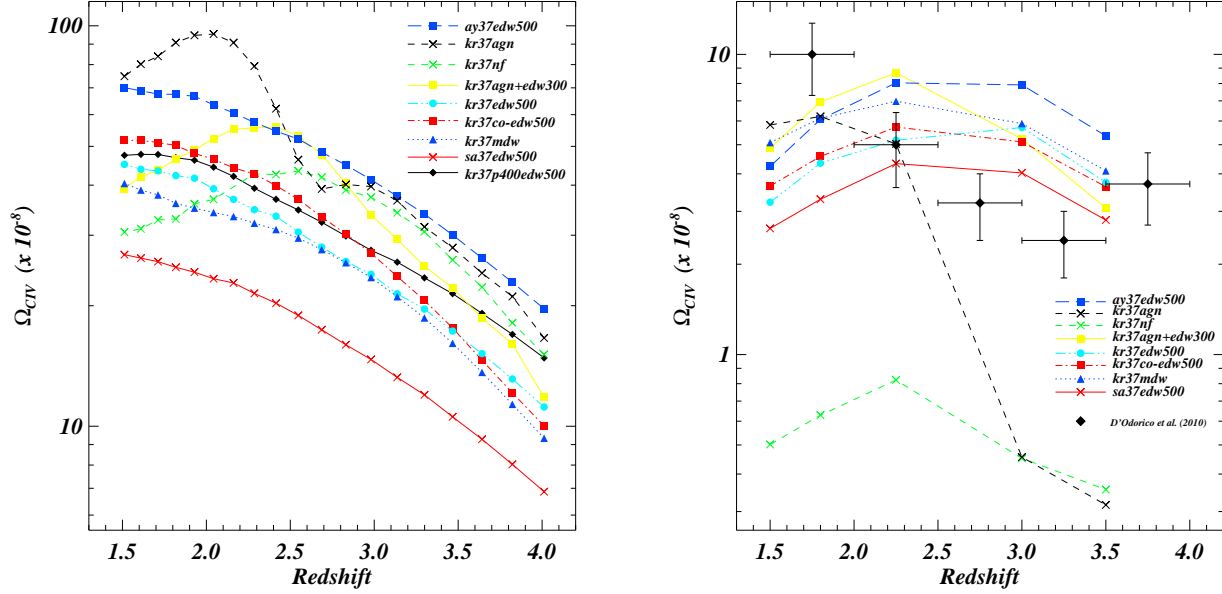


Figure 11. As in Figure 9, but at redshift  $z = 1.5$ .



**Figure 12.** *Left Panel:* evolution of the total  $\Omega_{\text{CIV}}$  as a function of redshift for all the hydrodynamic simulations of Table 2. *Right Panel:*  $\Omega_{\text{CIV}}$  evolution with redshift, calculated considering the absorption lines in 1000 lines-of-sight through each box, for the different simulation boxes. The overplotted black diamonds show the observational data of D’Odorico et al. (2010).

range of column densities. From  $z = 3.5$  to  $z = 2.5$  all the simulations, except for the kr37nf (no-feedback) and the kr37agn (AGN-feedback), roughly reproduce the observational data and show an increasing or constant trend for the  $\Omega_{\text{CIV}}$ . Down to redshift  $z = 3$  the AGN feedback of run kr37agn is not active and the CIV content is nearly equal to the one of the no-feedback simulation kr37nf. At  $z = 3$  the AGN feedback starts to work and the kr37agn run suddenly reaches all the other “wind” simulations.

Apart from the no-feedback simulation kr37nf (green crosses and dashed line), all the other runs still reproduce the observational data around redshift  $z = 2.25 \pm 0.25$ . If we consider lower redshift, all the simulations show a decreasing trend at variance with the data. Different is the case of the kr37agn run: from redshift  $z = 3.0$  to 1.8, the AGN feedback suppresses efficiently the star formation, therefore the gas is no longer reprocessed from the stars and the CIV is not converted in other ions. At the same time, the AGN feedback has not yet made the haloes devoid of gas, with the result that  $\Omega_{\text{CIV}}$  continues to increase. However, since the black holes accretion feedback is extremely powerful, moving to lower redshift a considerable amount of gas is expelled from the haloes and heated. As a consequence  $\Omega_{\text{CIV}}$  starts to decrease, even if at a later time and to a smaller degree than the “wind” runs.

## 8 PROBABILITY DISTRIBUTION FUNCTION OF THE CIV DOPPLER PARAMETER

In this Section we focus on the CIV Doppler parameter probability distribution function, plotted at redshift  $z = 3$ , 2.25 and 1.5 in Figures 13, 14 and 15, respectively. The data from D’Odorico et al. (2010) are also overplotted in these figures with a purple solid line along with the associated Poissonian error (shaded region). For this analysis we considered CIV *lines*.

At redshift  $z = 3$  (Figure 13) all the runs are quite in agreement with the data even if there are some small discrepancies. All

the runs tend to underestimate the observed distribution in the first bin,  $b_{\text{CIV}} < 4 \text{ km s}^{-1}$ , and slightly overestimate it for  $b_{\text{CIV}} > 28 \text{ km s}^{-1}$ . In the intermediate range  $4 < b_{\text{CIV}} < 28 \text{ km s}^{-1}$ , the simulations behave differently. The kr37mdw, kr37agn+edw300, kr37co-edw500 (left panel) and sa37edw500 (right panel) runs fit very well the observational data, while runs kr37edw500 and ay37edw500 (right panel) overproduce the observed distribution in the bin centered at  $b_{\text{CIV}} = 10 \text{ km s}^{-1}$ . Again the runs kr37nf and kr37agn show a different trend with respect to the others, for exactly the same reasons mentioned in the previous sections. Simulations kr37nf (no-feedback, right panel green dashed line) and kr37agn (AGN-feedback, left panel black dashed line) distributions are shifted towards higher  $b_{\text{CIV}}$  than the observed one. At this redshift AGN feedback is not active so, as the no-feedback case of kr37nf, the gas remains trapped inside haloes at high density and temperature. Run kr37p400edw500 show a marked excess of low CIV Doppler parameters due to its improved resolution that can resolve higher densities at earlier times and produces a lot of small metal enriched clumps in the IGM. At  $z = 3$ , the median value of the observational Doppler parameters distribution is  $9.88 \text{ km s}^{-1}$ , while the simulations have median ranging from  $8.49 \text{ km s}^{-1}$  (kr37p400edw500) to  $13.03 \text{ km s}^{-1}$  (kr37nf).

The situation is different at redshift  $z = 2.25$  (Figure 14) and  $z = 1.5$  (Figure 15). Moving to lower redshift, all the simulations show an excess of low Doppler parameters ( $b_{\text{CIV}} < 8 \text{ km s}^{-1}$ ), and also they underproduce the observed distribution in the range  $8 < b_{\text{CIV}} < 20 \text{ km s}^{-1}$ . Moreover, while at low redshift the kr37nf simulation (no-feedback, right panels green dashed lines) is still shifted towards higher  $b_{\text{CIV}}$  with respect to the observed distribution, the kr37agn run (AGN-feedback, left panels black dashed lines) at redshift  $z = 2.25$  fits better the data and it finally approaches all the other runs at  $z = 1.5$ , further confirming the increasing efficiency of the AGN feedback at low redshift. At  $z = 2.25$  and  $z = 1.5$ , the data by D’Odorico et al. (2010) have

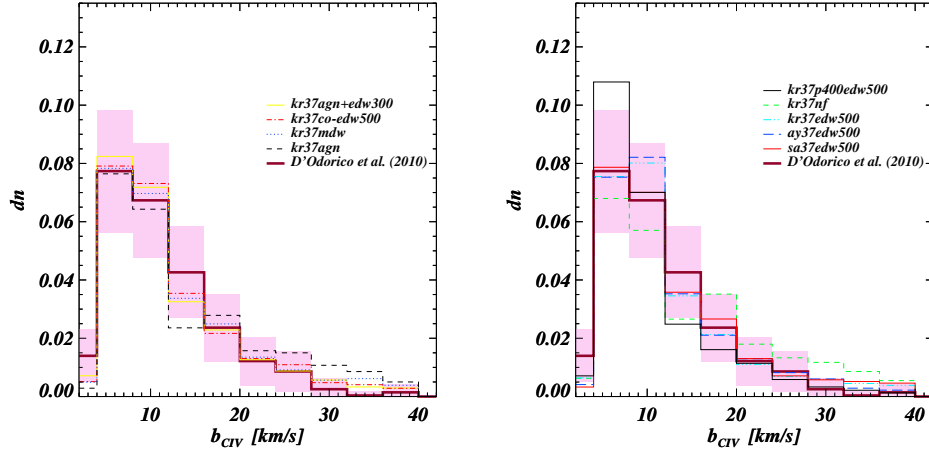


**Figure 13.** Line-widths  $b_{\text{CIV}}$  probability distribution function at  $z = 3$ . *Left panel:* part I. *Right panel:* part II. In both panels, data from D’Odorico et al. (2010) are showed by the purple solid line along with the associated Poissonian error (shaded region).

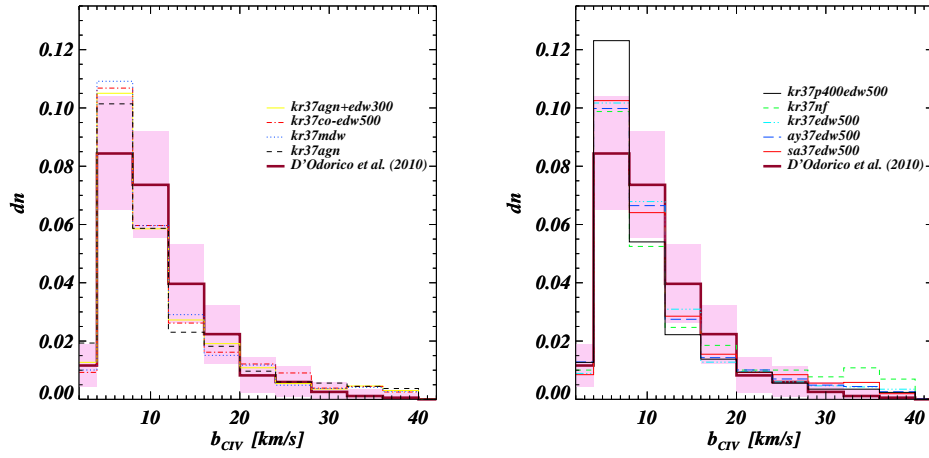


**Figure 14.** As in Figure 13, but at redshift  $z = 2.25$ .

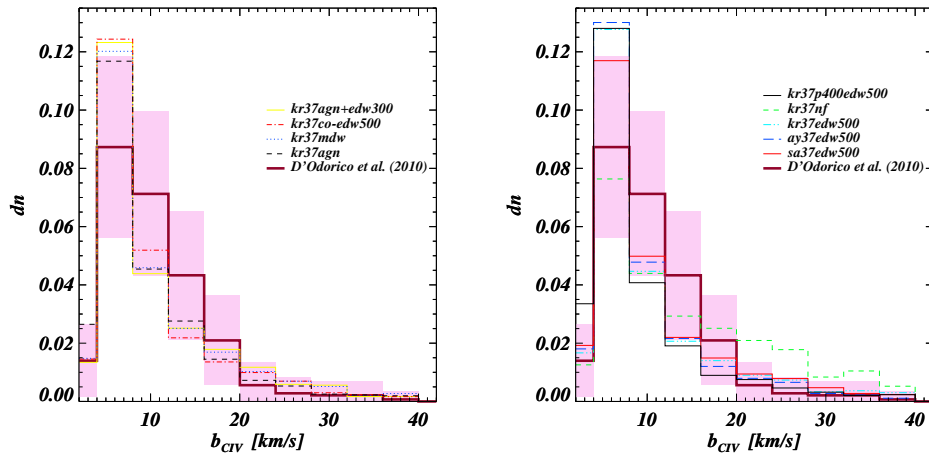


**Figure 15.** As in Figure 13, but at redshift  $z = 1.5$ .

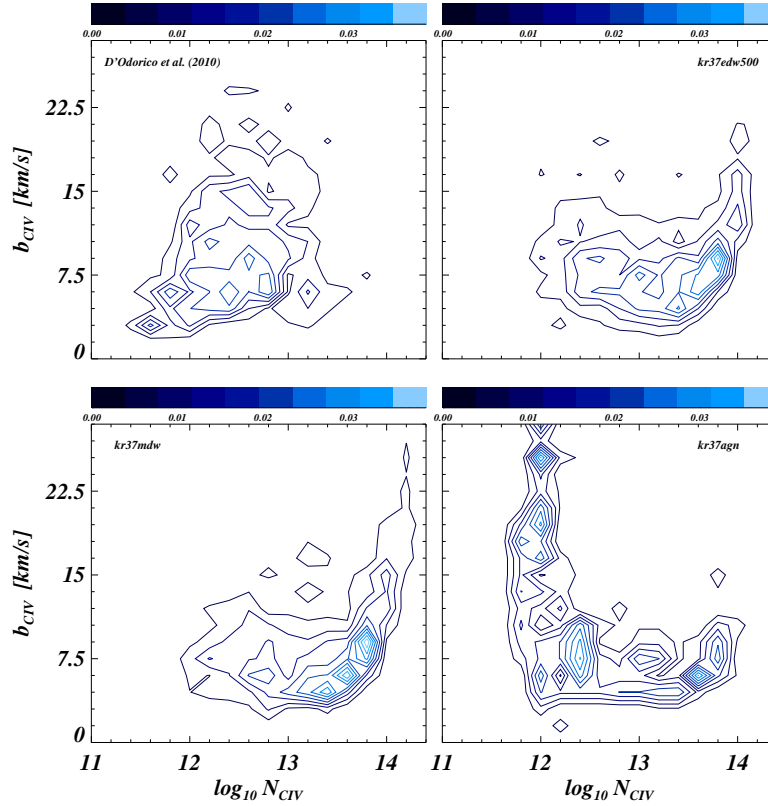


**Figure 16.**  $b_{\text{CIV}} - N_{\text{CIV}}$  relation at  $z = 3$ . The horizontal bars are colour coded according to the fraction of points that fall in each bin with coordinate  $(b_{\text{CIV}}, N_{\text{CIV}})$ . Upper left panel: observational data from D’Odorico et al. (2010).

median value respectively equal to  $9.30$  and  $9.25 \text{ km s}^{-1}$ , while the simulations have median around, respectively,  $8.55$  and  $7.40 \text{ km s}^{-1}$  ( $12.47 \text{ km s}^{-1}$  in the case of the no-feedback run kr37nf).

We stress that the small discrepancy between observed and simulated distributions for low Doppler parameters ( $b_{\text{CIV}} < 8 \text{ km s}^{-1}$ ) appears in a range that is influenced by the adopted resolution (remember that we have convolved the simulated spectra with a Gaussian of  $6.6 \text{ km s}^{-1}$  FWHM) and a slightly different value than the one used could alleviate this discrepancy

Compared to that of HI, the CIV Doppler parameter distribution function is less affected by the choice of the UV background (and in particular of the factor of 3.3 discussed in Sections 3 and 5.2). This is due to the fact that CIV absorption is related to higher density regions (mainly the outskirts of galactic haloes) than the HI absorption. In these regions, the impact of the IGM local temperature and density on the ionization state of Carbon is considerably more important than the UVB contribution.

## 9 THE CIV COLUMN DENSITY-DOPPLER PARAMETER RELATION

In Figures 16, 17 and 18 we plot the  $b_{\text{CIV}} - N_{\text{CIV}}$  relation, at redshift  $z = 3$ ,  $z = 2.25$  and  $z = 1.5$  respectively, for the reference simulations kr37edw500, kr37mdw and kr37agn. The contour plots are colour coded according to the fraction of points that fall in each bin with coordinate  $(b_{\text{CIV}}, N_{\text{CIV}})$ . In the upper left panel of the figures the observational data of D’Odorico et al. (2010) are plotted. As in the previous Section, we considered here CIV *lines*.

At redshift  $z = 3$  (Figure 16), the data distributions of runs

kr37edw500 (energy-driven winds) and kr37mdw (momentum-driven winds) are in agreement with each other but are quite different from the observed one. In particular the simulated distributions are shifted towards higher CIV column densities and are concentrated around a narrower region than the observational data. The low column density tail of the distributions is completely missing, while the high column density tail shows a sort of correlation between the CIV Doppler parameters and  $N_{\text{CIV}}$ . We interpret this latter as a  $T - \rho$  relation: lines with higher column densities (i.e. associated to denser regions) have higher Doppler parameters (i.e. temperature). The fact that this relation appears only at high column densities is not a surprise: for high values of  $N_{\text{CIV}}$ , absorption lines are very strong and well resolved, so they are good tracers of the physical state of the intergalactic gas and also they are better fit by VPFIT. The case of run kr37agn is different: in fact the  $T - \rho$  relation for large  $N_{\text{CIV}}$  values is missing, while a clump of systems with a large spread in  $b_{\text{CIV}}$  values at low column density is clearly visible. This distribution results because, at redshift  $z = 3$ , in the kr37agn run the gas resides inside the high density high temperature cores of the haloes where it is reprocessed by the stars, and the amount of diffused CIV is rather low (see the right panel of Figure 12). Therefore, since the CIV absorption lines are weak and not well defined, the quality of the fit made by VPFIT is rather poor. As we reported in Section 5.2, in such a case VPFIT tends to add broad components in order to minimize the  $\chi^2$  statistics and this results in the feature of spurious systems at low column density shown in the lower right panel of Figure 16. While the effect is less evident (but present) for the other runs or in the case of the  $b_{\text{HI}} - N_{\text{HI}}$  relation, it is now much more prominent. Of course, observational data do not



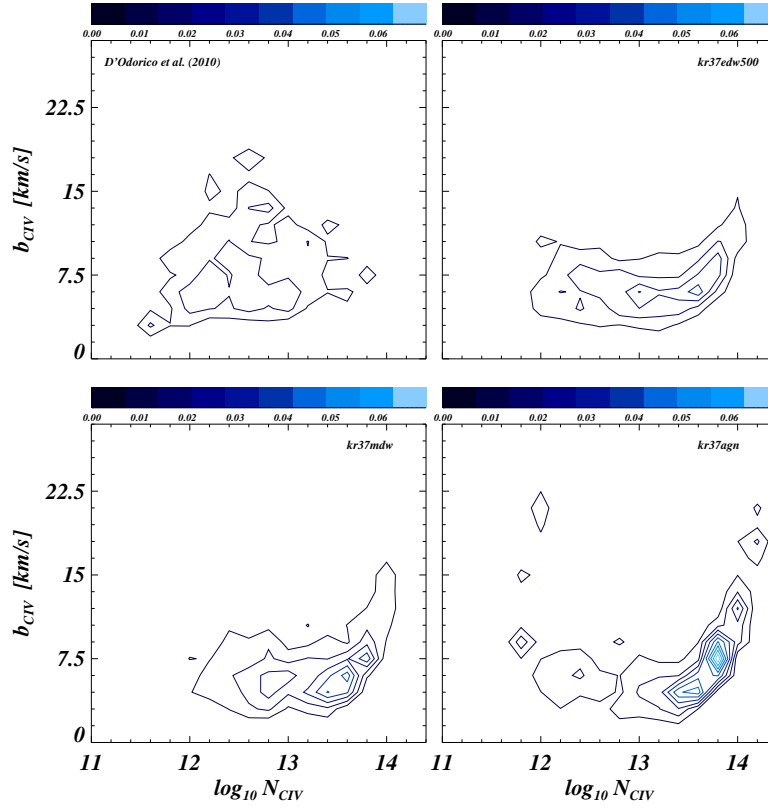


Figure 17. As in Figure 16, but at redshift  $z = 2.25$ .

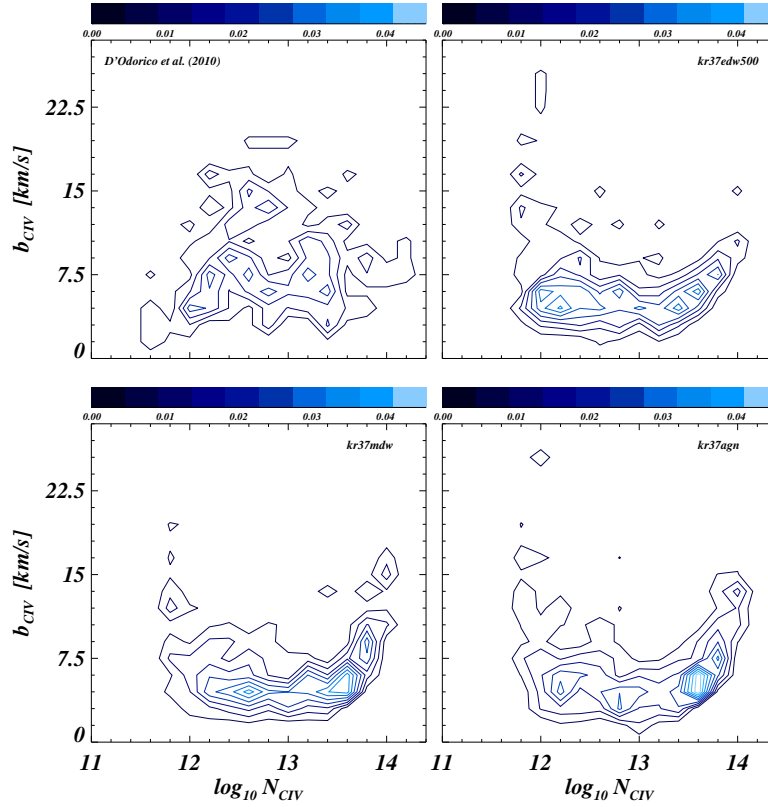


Figure 18. As in Figure 16, but at redshift  $z = 1.5$ .

present such a feature, because in the “by eye” procedure of fitting these spurious lines are removed.

At redshift  $z = 2.25$  (Figure 17) and  $z = 1.5$  (Figure 18) the kr37agn run approaches the other two simulations. The  $b_{\text{CIV}} - N_{\text{CIV}}$  correlation at high column densities is now present for all the runs but the simulated distributions are still different from the observed one. The clump of low density systems disappears almost completely at  $z = 2.25$ , but is visible also for the runs kr37edw500 and kr37mdw at redshift  $z = 1.5$ . There is a simple reason for this: at low redshift the amount of CIV, traced by random line-of-sight along the box, decreases (right panel of Figure 12), while the number of low column density systems significantly increases (Figure 11) and typically these lines have a large spread in their Doppler parameter value.

The difference between simulated and observed distributions could also be due to the fact that simulated haloes, and in particular their outskirts, can have different properties from that of the observed ones: for example this is also seen from the SiII statistics in DLA systems that appear to be not in agreement with observations. Although in the present paper we explore the effect of feedback, there might be other physical effects that can contribute as well in shaping the properties of the  $b_{\text{CIV}} - N_{\text{CIV}}$  distribution.

## 10 $N_{\text{CIV}} - N_{\text{HI}}$ CORRELATED ABSORPTION

The last part of this work is dedicated to the HI-CIV correlated absorption. We define as correlated absorption HI-CIV systems in which CIV and HI are physically dependent or, in other words, related to the same absorptive structure. In real spectra, however, two absorbers each containing CIV could be very close in redshift space but far in real space due to the bulk motions and the peculiar velocity. For this reason there are often serious problem on how to associate each CIV components to physically corresponding HI components. In this Section, besides the data of D’Odorico et al. (2010), we compare with the fitting formulae obtained from the Kim et al. (2010) data. In order to do that, only for this analysis we changed the velocity range,  $dv_{\text{min}}$ , used so far to define *systems* of lines. Following Kim et al. (2010) and differently from what was done in Sections 6 and 7, where we set  $dv_{\text{min}} = 50 \text{ km s}^{-1}$ , we use here the velocity interval  $[-250 \text{ km s}^{-1}, 250 \text{ km s}^{-1}]$  both for the simulated and the observed CIV and HI systems.

In Figures 19 and 20 we show our findings for some of the simulations in Table 2 and for the D’Odorico et al. (2010) data. The red-dashed and yellow-solid curves represent the Kim et al. (2010) fit, obtained by using the function:

$$\log N_{\text{CIV}} = \left[ \frac{C_1}{\log N_{\text{HI}} + C_2} \right] + C_3. \quad (20)$$

The parameters for the red-dashed curves are:  $C_1 = [-4.43 \pm 1.30, -7.57 \pm 1.80]$ ,  $C_2 = [-13.04 \pm 0.44, -12.45 \pm 0.45]$ ,  $C_3 = [15.22 \pm 0.17, 15.65 \pm 0.19]$  at  $z = [2.25, 3.0]$ . These red-dashed curves represent a fit to *all* the Kim et al. (2010) data available at the two different redshifts. The parameters for the yellow-solid curves are:  $C_1 = [-2.01 \pm 0.35, -2.51 \pm 0.47]$ ,  $C_2 = [-14.22 \pm 0.14, -14.08 \pm 0.20]$ ,  $C_3 = [14.96 \pm 0.05, 15.09 \pm 0.07]$  at  $z = [2.25, 3.0]$ . These curves represent an improved fit made to reproduce better the clump of systems at low  $N_{\text{HI}}$  and low  $N_{\text{CIV}}$ .

At redshift  $z = 3$  (Figure 19) for the D’Odorico et al. (2010) observational data and for the kr37agn+edw300, kr37edw500 and kr37mdw runs the bulk of systems is located at  $\log N_{\text{HI}} (\text{cm}^{-2}) < 16$  and it follows the Kim et al. (2010) fitting functions, even if with

a slightly steeper trend, while at  $\log N_{\text{HI}} (\text{cm}^{-2}) > 16$  the spread in the simulated data increases (also the data of Kim et al. 2010, present a sort of bimodality with high HI column density distribution more spread than the tight low HI column density one). Runs kr37nf (no-feedback) and kr37agn (AGN-feedback) at this redshift behave similarly: they do not show the  $\log N_{\text{HI}} (\text{cm}^{-2}) < 16$  CIV-HI correlation above, and the  $\log N_{\text{HI}} (\text{cm}^{-2}) > 16$  systems are rare. All the simulations show a strip of values with  $\log N_{\text{HI}} (\text{cm}^{-2}) < 15$  and  $\log N_{\text{CIV}} (\text{cm}^{-2}) \sim 12$ . This is due to the VPFIT spurious line fitting effect described in the previous Section. In fact, it is particular evident for the runs kr37nf and kr37agn, because in these two cases the amount of the diffuse CIV is lower and the CIV absorption lines are weak and not well defined.

At redshift  $z = 2.25$  (Figure 20) the above trends are in place even if all the simulated distributions are now shifted towards slightly lower HI column densities with respect to the fitting functions of Kim et al. (2010). Otherwise, the number of components of the D’Odorico et al. (2010) data increases at this redshift and the bulk of systems at  $\log N_{\text{HI}} (\text{cm}^{-2}) < 16$  is well fitted by the functions of Kim et al. (2010). Again, moving to lower redshift, the simulation with AGN feedback, kr37agn, starts to follow the other wind runs.

To summarize, two effects are visible from the plots: (a) for a given  $N_{\text{HI}}$ , the scatter in the corresponding  $N_{\text{CIV}}$  is broader, and the  $N_{\text{CIV}}$  values typically larger, than what is inferred from observations; (b) the simulated distributions of  $N_{\text{HI}}$  are slightly lower compared to the Kim et al. (2010) fitting functions and the D’Odorico et al. (2010) data at redshift  $z = 2.25$ .

## 11 CONCLUSIONS AND DISCUSSION

In this paper we investigated the global properties of triply ionized Carbon (CIV) as an IGM tracer at  $z \geq 1.5$ . From the numerical point of view we presented the results of a new set of hydrodynamic simulations that incorporate feedback either in the form of galactic winds or in the form of energy from black holes accretion (AGN feedback). From the observational point of view we relied on recent high-resolution data sets obtained with the UVES spectrograph at VLT and the HIRES spectrograph at Keck. The main results can be summarized as follows:

- The statistics of HI are weakly affected by the feedback prescription implemented: both the column density distribution function and the Doppler width distributions do not change significantly when considering the different simulations. We regard this as a geometrical effect: winds and AGN feedback are stronger at the intersection of IGM filaments and these sites have usually small filling factor. Only the high column density tail shows small differences between the runs considered (Section 5). The fact that overall our simulations reproduce well all the HI statistics confirms that we are catching the physics of the gas traced by the neutral hydrogen. The remaining small discrepancies with the observational data could be due to the UV background we used (Haardt & Madau 1996, produced by quasars and galaxies, with the heating rates multiplied by a factor of 3.3), that heats too much the gas. In minor part, the discrepancies are also due to a numerical effect introduced by the line-fitting software VPFIT.

- Compared to that of HI, the statistics of CIV is strongly affected by feedback. If we consider *systems* of lines as defined in Section 2, at redshift  $z = 3, 2.25$  and  $1.5$ , all the simulations except for the no-feedback run kr37nf and the AGN-feedback run kr37agn

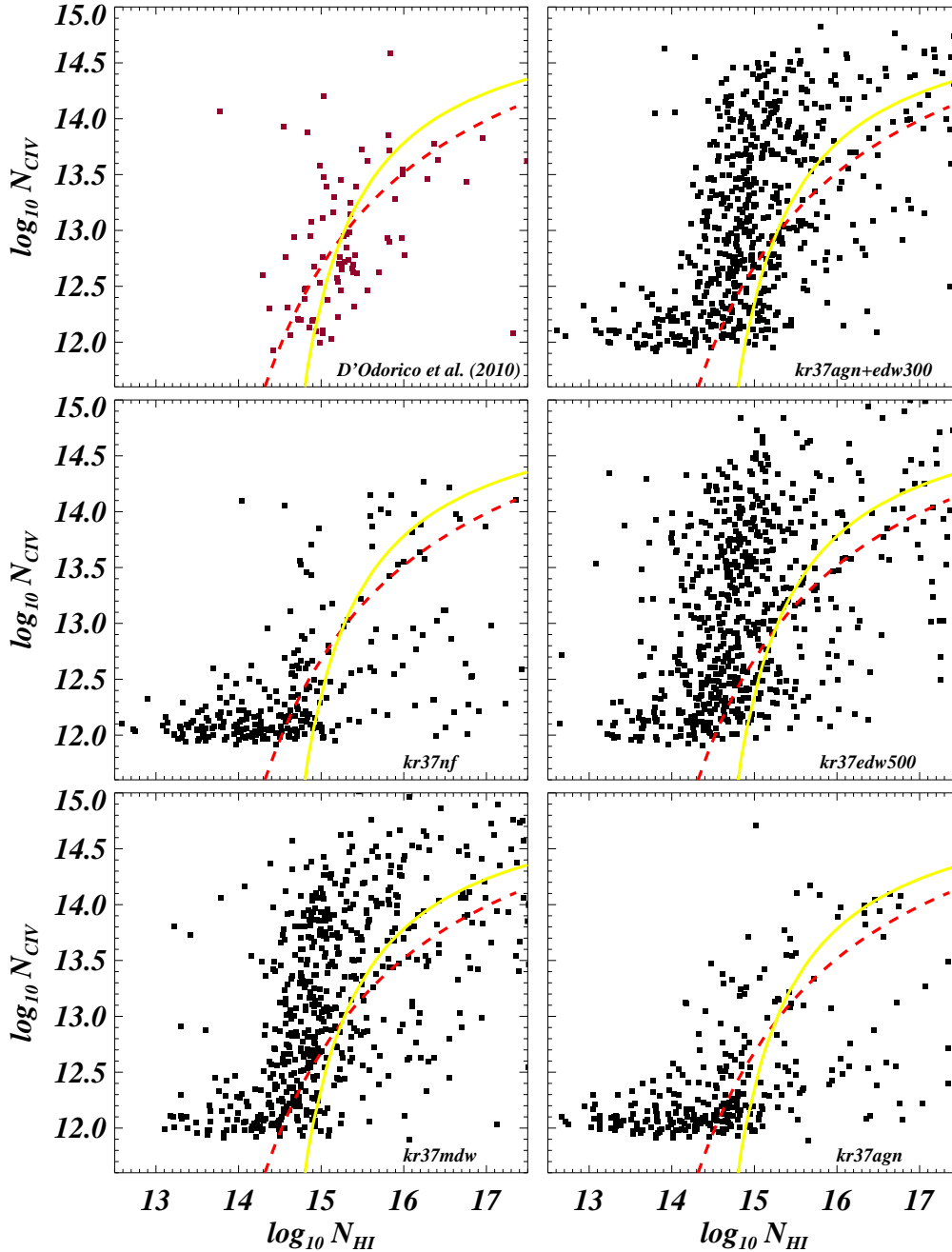


**Figure 19.** Column densities  $N_{\text{CIV}} - N_{\text{HI}}$  correlated absorption for systems at  $z = 3$ . Upper left panel: observational data from D’Odorico et al. (2010). The red-dashed and yellow-solid curves represent the fitting functions of Kim et al. (2010).

(this latter only at high redshift) agree with the observed CIV column density distribution function. Galactic winds feedback starts to be active at high redshift, but moving to lower redshift, also the AGN feedback becomes effective and the kr37agn simulation follows all the other wind runs (see Figures 9, 10 and 11).

- In the second part of Section 7, we presented the evolution with redshift of the CIV cosmological mass density, calculated considering the column density distribution function of the CIV absorption lines. In the redshift range  $z = 2.5 - 3.5$ , our simulations, except for the no-feedback run kr37nf and the AGN-feedback

run kr37agn, reproduce the observed  $\Omega_{\text{CIV}}(z)$  evolution, even if with a slightly overestimation, and they perfectly reproduce the observational data around redshift  $z = 2.25 \pm 0.25$ . At lower redshift we found a decreasing trend at variance with the increasing trend shown by the observational data (right panel of Figure 12). In the AGN case the trend is nearly constant at low redshift and in better agreement with data. We think that a better calibration of the coupled AGN + galactic winds feedback model of run kr37agn+edw300 could help to improve this result.

- At all the redshift considered, the CIV Doppler parameter dis-

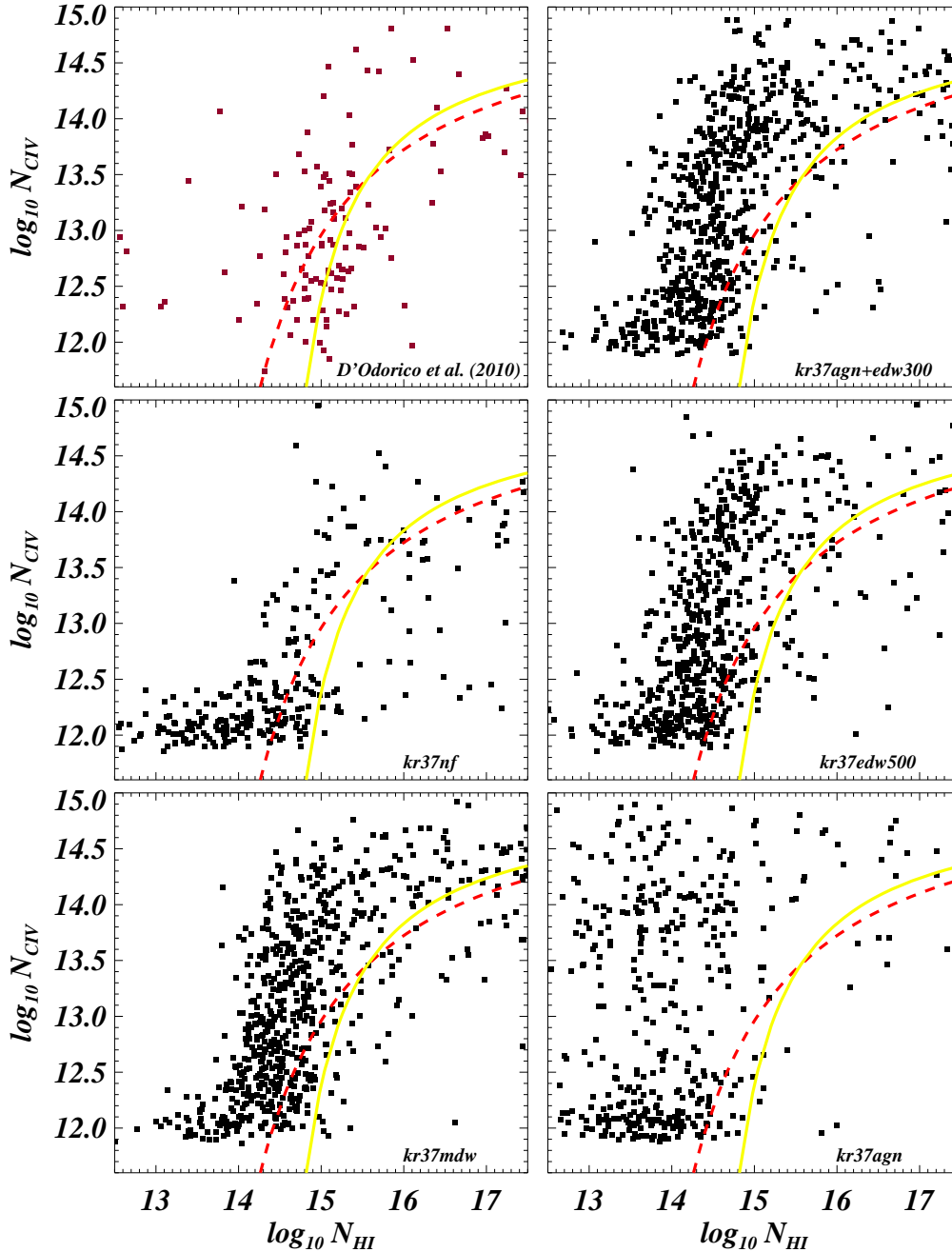


**Figure 20.** As in Figure 19, but at redshift  $z = 2.25$ .

tribution is in good agreement with the observational data. The no-feedback and AGN-feedback simulations (the latter only at high redshift) result in distributions shifted towards higher  $b_{\text{CIV}}$  than the observed ones: this is due to the fact that these runs produce gas around galaxies that is too hot than what was inferred from observations (Section 8).

- The overall  $b_{\text{CIV}} - N_{\text{CIV}}$  data distribution of our reference simulations is different from the observed one. The high column density tail of all the runs considered (but for the AGN-feedback run this is true only at low redshift) shows a sort of correlation between the CIV Doppler parameters and the column density, in

which the Doppler parameters increase as  $N_{\text{CIV}}$  increases: the sign of a well defined temperature-density relation for the high density gas. Especially at low redshift, when the amount of CIV traced by random line-of-sight along the box decreases, a clump of systems with a huge scatter in the  $b_{\text{CIV}}$  values at low CIV column density is present. This effect should be regarded as of numerical origin and it is introduced by VPFIT when fitting regions close to the continuum in the mock data set (Section 9). A more careful comparison between data and simulations is needed in order to address this effect at a more quantitative level.

- In Section 10 we explored the correlated CIV-HI absorption,

considering *systems* of lines in which CIV and HI are physically dependent. At the two redshift considered,  $z = 3$  and  $z = 2.25$ , both our reference runs and the observational data of D’Odorico et al. (2010) roughly follow the fit proposed by Kim et al. (2010), even if the simulations show a slightly steeper trend in the range  $\log N_{\text{HI}} (\text{cm}^{-2}) < 16$ .

- Even if we are not able to fit all the statistics at once if we consider the neutral hydrogen HI and the triply ionized Carbon CIV, momentum-driven winds simulation reproduce best all the different quantities explored in this paper (as found for Damped Lyman- $\alpha$  systems by Tescari et al. 2009, and for IGM metal lines by Oppenheimer & Davé 2006, 2008).

- To sum up, feedback appears to be a crucial physical ingredient in order to reproduce statistics of metal absorption lines. In particular, the effect of galactic winds triggered by supernovae is important at high redshift, while the effect of black holes accretion feedback starts to become prominent at  $z < 3$ . However, because the AGN feedback is very strong, it will be crucial to improve the coupled AGN + galactic winds model, where the effect of the winds at high redshift reduces the strength of the black holes accretion at low redshift.

In our analysis, we found two different effects biasing the statistics related to the HI and CIV absorption lines: the choice of the UV background and the VPFIT lines fitting procedure. In the future we will try to improve these statistics by using a more physically motivated UV background that takes into account HeII reionization at  $z \sim 3$ . Furthermore, we will try to improve our automatic line-fitting analysis by removing numerical artifacts introduced by VPFIT, since the automatic fitting procedure is not likely to be as accurate as a “by eye” fitting made by an observer, and introduce spurious lines especially in the continuum region. Our results can also be tested by using other statistics based on pixel-optical depths techniques.

A second possible improvement of the results presented in this paper is the refinement of the feedback models and the inclusion of new physical processes like turbulence, metal diffusion and radiative transfer, that can help in polluting with metals the low-density IGM. So far we explored feedback prescriptions in the form of energy-driven galactic winds (EDW), momentum-driven galactic winds (MDW) and black holes accretion (AGN feedback). Exploring the combined effect of these models seems to be promising: for example the “energy coupled momentum driven winds” model by Choi & Nagamine (2010) succeeds in enriching the gas (like the EDW model) without heating too much the IGM (like the MDW model). The modelization inside the hydrodynamic simulations of the radiative transfer is fundamental and could also impact on the metal mixing. Finally, it will be crucial to incorporate in the GADGET-2 code the small-scale turbulence and its impact on the metal diffusion at large scales. With physical mixing, fluid elements on a fixed (resolved) physical scale do exchange energy/entropy due to unresolved (turbulent) motions: diffusion allows some ejecta gas to mix while exiting the galaxies (Shen et al. 2010). All the previous effects, once included in simulations, could help in improving our understanding of the chemical and physical evolution of the IGM and provide a more comprehensive framework of the high-redshift galaxy/IGM interplay.

## ACKNOWLEDGMENTS

Numerical computations were done on the COSMOS (SGI Altix 3700) supercomputer at DAMTP and at High Performance Com-

puter Cluster (HPCF) in Cambridge (UK) and at CINECA (Italy). COSMOS is a UK-CCC facility which is supported by HEFCE, PPARC and Silicon Graphics/Cray Research. The CINECA (“Centro Interuniversitario del Nord Est per il Calcolo Elettronico”) CPU time has been assigned thanks to an INAF-CINECA grant. This work has been partially supported by the INFN-PD51 grant, an ASI-AAE Theory grant and a PRIN-MIUR.

## REFERENCES

- Adelberger K. L., Shapley A. E., Steidel C. C., Pettini M., Erb D. K., Reddy N. A., 2005, *ApJ*, 629, 636
- Aguirre A., Schaye J., Hernquist L., Kay S., Springel V., Theuns T., 2005, *ApJ*, 620, L13
- Aracil B., Petitjean P., Pichon C., Bergeron J., 2004, *A&A*, 419, 811
- Arimoto N., Yoshii Y., 1987, *A&A*, 173, 23
- Asplund M., Grevesse N., Sauval A. J., 2005, in Barnes III T. G., Bash F. N., eds, *Cosmic Abundances as Records of Stellar Evolution and Nucleosynthesis Vol. 336 of Astronomical Society of the Pacific Conference Series, The Solar Chemical Composition*. pp 25–
- Becker G. D., Rauch M., Sargent W. L. W., 2009, *ApJ*, 698, 1010
- Bergeron J., Petitjean P., Aracil B., Pichon C., Scannapieco E., Srianand R., Boisse P., Carswell R. F., Chand H., Cristiani S., Ferrara A., Haehnelt M., Hughes A., Kim T., Ledoux C., Richter P., Viel M., 2004, *The Messenger*, 118, 40
- Bertone S., Schaye J., Booth C. M., Dalla Vecchia C., Theuns T., Wiersma R. P. C., 2010, *MNRAS*, 408, 1120
- Bertone S., Schaye J., Dalla Vecchia C., Booth C. M., Theuns T., Wiersma R. P. C., 2010, *MNRAS*, 407, 544
- Boksenberg A., Sargent W. L. W., Rauch M., 2003, *ArXiv Astrophysics e-prints*
- Bolton J. S., Haehnelt M. G., 2007, *MNRAS*, 374, 493
- Bolton J. S., Haehnelt M. G., Viel M., Springel V., 2005, *MNRAS*, 357, 1178
- Bondi H., 1952, *MNRAS*, 112, 195
- Booth C. M., Schaye J., 2009, *MNRAS*, 398, 53
- Calura F., Matteucci F., 2006, *MNRAS*, 369, 465
- Calura F., Menci N., 2009, *MNRAS*, 400, 1347
- Cen R., Chisari N. E., 2010, *ArXiv e-prints*
- Cen R., Nagamine K., Ostriker J. P., 2005, *ApJ*, 635, 86
- Choi J., Nagamine K., 2010, *MNRAS*, pp 1614–
- Cowie L. L., Songaila A., Kim T., Hu E. M., 1995, *AJ*, 109, 1522
- Dalla Vecchia C., Schaye J., 2008, *MNRAS*, 387, 1431
- Davé R., Oppenheimer B. D., Katz N., Kollmeier J. A., Weinberg D. H., 2010, *MNRAS*, 408, 2051
- Dekker H., D’Odorico S., Kaufer A., Delabre B., Kotzlowski H., 2000, in M. Iye & A. F. Moorwood ed., *Society of Photo-Optical Instrumentation Engineers (SPIE) Conference Series Vol. 4008 of Society of Photo-Optical Instrumentation Engineers (SPIE) Conference Series, Design, construction, and performance of UVES, the echelle spectrograph for the UT2 Kueyen Telescope at the ESO Paranal Observatory*. pp 534–545
- Di Matteo T., Colberg J., Springel V., Hernquist L., Sijacki D., 2008, *ApJ*, 676, 33
- Di Matteo T., Springel V., Hernquist L., 2005, *Nat*, 433, 604
- D’Odorico V., Bruscoli M., Saitta F., Fontanot F., Viel M., Cristiani S., Monaco P., 2008, *MNRAS*, 389, 1727
- D’Odorico V., Calura F., Cristiani S., Viel M., 2010, *MNRAS*, 401, 2715

- D’Odorico V., Petitjean P., Cristiani S., 2002, *A&A*, 390, 13
- Fabjan D., Borgani S., Tornatore L., Saro A., Murante G., Dolag K., 2010, *MNRAS*, 401, 1670
- Faucher-Giguère C.-A., Lidz A., Hernquist L., Zaldarriaga M., 2008, *ApJ*, 688, 85
- Ferland G. J., Korista K. T., Verner D. A., Ferguson J. W., Kingdon J. B., Verner E. M., 1998, *PASP*, 110, 761
- Fontana A., Ballester P., 1995, *The Messenger*, 80, 37
- Haardt F., Madau P., 1996, *ApJ*, 461, 20
- Haehnelt M. G., Steinmetz M., Rauch M., 1996, *ApJ*, 465, L95+
- Katz N., Weinberg D. H., Hernquist L., 1996, *ApJS*, 105, 19
- Kawata D., Rauch M., 2007, *ApJ*, 663, 38
- Kim T., Bolton J. S., Viel M., Haehnelt M. G., Carswell R. F., 2007, *MNRAS*, 382, 1657
- Kim T.-S., Partl A. M., Carswell R. F., Mücke J., 2010, submitted to *MNRAS*, pp 1–36
- Kirkman D., Tytler D., 1997, *ApJ*, 484, 672
- Kobayashi C., Springel V., White S. D. M., 2007, *MNRAS*, 376, 1465
- Komatsu E., Dunkley J., Nolte M. R., Bennett C. L., Gold B., Hinshaw G., Jarosik N., Larson D., Limon M., Page L., Spergel D. N., Halpern M., Hill R. S., Kogut A., Meyer S. S., Tucker G. S., Weiland J. L., Wollack E., Wright E. L., 2009, *ApJS*, 180, 330
- Kroupa P., 2001, *MNRAS*, 322, 231
- Lesgourgues J., Viel M., Haehnelt M. G., Massey R., 2007, *Journal of Cosmology and Astro-Particle Physics*, 11, 8
- Martin C. L., 2005, *ApJ*, 621, 227
- Murray N., Quataert E., Thompson T. A., 2005, *ApJ*, 618, 569
- Nagamine K., Springel V., Hernquist L., 2004, *MNRAS*, 348, 435
- Oppenheimer B. D., Davé R., 2006, *MNRAS*, 373, 1265
- Oppenheimer B. D., Davé R., 2008, *MNRAS*, 387, 577
- Oppenheimer B. D., Davé R., Finlator K., 2009, *MNRAS*, 396, 729
- Padovani P., Matteucci F., 1993, *ApJ*, 416, 26
- Pichon C., Scannapieco E., Aracil B., Petitjean P., Aubert D., Bergeron J., Colombi S., 2003, *ApJ*, 597, L97
- Pieri M. M., Schaye J., Aguirre A., 2006, *ApJ*, 638, 45
- Porciani C., Madau P., 2005, *ApJ*, 625, L43
- Ricotti M., Gnedin N. Y., Shull J. M., 2000, *ApJ*, 534, 41
- Rupke D. S., Veilleux S., Sanders D. B., 2005, *ApJS*, 160, 115
- Ryan-Weber E. V., Pettini M., Madau P., 2006, *MNRAS*, 371, L78
- Ryan-Weber E. V., Pettini M., Madau P., Zych B. J., 2009, *MNRAS*, 395, 1476
- Saitta F., D’Odorico V., Bruscoli M., Cristiani S., Monaco P., Viel M., 2008, *MNRAS*, 385, 519
- Salpeter E. E., 1955, *ApJ*, 121, 161
- Scannapieco E., Pichon C., Aracil B., Petitjean P., Thacker R. J., Pogosyan D., Bergeron J., Couchman H. M. P., 2006, *MNRAS*, 365, 615
- Schaerer D., 2003, *A&A*, 397, 527
- Schaye J., 2001, *ApJ*, 559, 507
- Schaye J., Aguirre A., Kim T.-S., Theuns T., Rauch M., Sargent W. L. W., 2003, *ApJ*, 596, 768
- Schaye J., Rauch M., Sargent W. L. W., Kim T., 2000a, *ApJ*, 541, L1
- Schaye J., Theuns T., Rauch M., Efstathiou G., Sargent W. L. W., 2000b, *MNRAS*, 318, 817
- Seljak U., Zaldarriaga M., 1996, *ApJ*, 469, 437
- Shakura N. I., Sunyaev R. A., 1973, *A&A*, 24, 337
- Shen S., Wadsley J., Stinson G., 2010, *MNRAS*, 407, 1581
- Sijacki D., Pfrommer C., Springel V., Enßlin T. A., 2008, *MNRAS*, 387, 1403
- Simcoe R. A., Sargent W. L. W., Rauch M., Becker G., 2006, *ApJ*, 637, 648
- Sommer-Larsen J., Fynbo J. P. U., 2008, *MNRAS*, 385, 3
- Springel V., 2005, *MNRAS*, 364, 1105
- Springel V., Di Matteo T., Hernquist L., 2005, *MNRAS*, 361, 776
- Springel V., Hernquist L., 2003, *MNRAS*, 339, 289
- Steidel C. C., Erb D. K., Shapley A. E., Pettini M., Reddy N., Bogosavljević M., Rudie G. C., Rakic O., 2010, *ApJ*, 717, 289
- Storrie-Lombardi L. J., McMahon R. G., Irwin M. J., 1996, *MNRAS*, 283, L79
- Sutherland R. S., Dopita M. A., 1993, *ApJS*, 88, 253
- Tescari E., Viel M., Tornatore L., Borgani S., 2009, *MNRAS*, 397, 411
- Theuns T., Leonard A., Efstathiou G., Pearce F. R., Thomas P. A., 1998, *MNRAS*, 301, 478
- Theuns T., Viel M., Kay S., Schaye J., Carswell R. F., Tzanavaris P., 2002, *ApJ*, 578, L5
- Thielemann F.-K., Argast D., Brachwitz F., Hix W. R., Höflich P., Liebendörfer M., Martínez-Pinedo G., Mezzacappa A., Panov I., Rauscher T., 2003, *Nuclear Physics A*, 718, 139
- Tornatore L., Borgani S., Dolag K., Matteucci F., 2007, *MNRAS*, 382, 1050
- Tornatore L., Borgani S., Viel M., Springel V., 2010, *MNRAS*, 402, 1911
- Tytler D., Gleed M., Melis C., Chapman A., Kirkman D., Lubin D., Paschos P., Jena T., Crotts A. P. S., 2009, *MNRAS*, 392, 1539
- van den Hoek L. B., Groenewegen M. A. T., 1997, *A&A Supp.*, 123, 305
- Vikhlinin A., Kravtsov A. V., Burenin R. A., Ebeling H., Forman W. R., Hornstrup A., Jones C., Murray S. S., Nagai D., Quintana H., Voevodkin A., 2009, *ApJ*, 692, 1060
- Weymann R. J., Carswell R. F., Smith M. G., 1981, *ARA&A*, 19, 41
- Wiersma R. P. C., Schaye J., Dalla Vecchia C., Booth C. M., Theuns T., Aguirre A., 2010, *MNRAS*, 409, 132
- Wiersma R. P. C., Schaye J., Theuns T., Dalla Vecchia C., Tornatore L., 2009, *MNRAS*, 399, 574
- Woolsey S. E., Weaver T. A., 1995, *ApJ*, 101, 181